

Protostellar Outflows at the Earliest Stages (POETS)

I. Radio thermal jets at high resolution nearby H₂O maser sources

A. Sanna^{1,2}, L. Moscadelli³, C. Goddi⁴, V. Krishnan³, and F. Massi³

¹ Max-Planck-Institut für Radioastronomie, Auf dem Hügel 69, 53121 Bonn, Germany
e-mail: asanna@mpi-fr-bonn.mpg.de

² INAF, Osservatorio Astronomico di Cagliari, via della Scienza 5, 09047 Selargius (CA), Italy

³ INAF, Osservatorio Astrofisico di Arcetri, Largo E. Fermi 5, 50125 Firenze, Italy

⁴ Department of Astrophysics/IMAPP, Radboud University Nijmegen, PO Box 9010, NL-6500 GL Nijmegen, the Netherlands

Received 5 June 2018 / Accepted 16 July 2018

ABSTRACT

Context. Weak and compact radio continuum and H₂O masers are preferred tracers of the outflow activity nearby very young stars. **Aims.** We want to image the centimeter free-free continuum emission, in the range 1–7 cm (26–4 GHz), which arises in the inner few 1000 au from those young stars also associated with bright H₂O masers. We want to study the radio continuum properties in combination with the H₂O maser kinematics, in order to eventually quantify the outflow energetics powered by single young stars. **Methods.** We made use of the Karl G. Jansky Very Large Array (VLA) in the B configuration at K band, and in the A configuration at both Ku and C bands, in order to image the radio continuum emission towards 25 H₂O maser sites with an angular resolution and thermal rms of the order of 0.1 and 10 μJy beam⁻¹, respectively. These targets add to our pilot study of 11 maser sites presented in Moscadelli et al. (2016). The sample of H₂O maser sites was selected among those regions having an accurate distance measurement, obtained through maser trigonometric parallaxes, and H₂O maser luminosities in excess of 10⁻⁶ L_⊙. **Results.** We present high-resolution radio continuum images of 33 sources belonging to 25 star-forming regions. In each region, we detect radio continuum emission within a few 1000 au of the H₂O masers' position; 50% of the radio continuum sources are associated with bolometric luminosities exceeding 5 × 10³ L_⊙, including W33A and G240.32+0.07. We provide a detailed spectral index analysis for each radio continuum source, based on the integrated fluxes at each frequency, and produce spectral index maps with the multi-frequency-synthesis deconvolution algorithm of CASA. The radio continuum emission traces thermal bremsstrahlung in (proto)stellar winds and jets, with flux densities at 22 GHz below 3 mJy, and spectral index values between -0.1 and 1.3. We prove a strong correlation ($r > 0.8$) between the radio continuum luminosity (L_{rad}) and the H₂O maser luminosity ($L_{\text{H}_2\text{O}}$) of $(L_{8\text{GHz}}/\text{mJy kpc}^2) = 10^{5.8} \times (L_{\text{H}_2\text{O}}/L_{\odot})^{0.74}$. This power-law relation is similar to that between the radio continuum and bolometric luminosities, which confirms earlier studies. Since H₂O masers are excited through shocks driven by (proto)stellar winds and jets, these results provide support to the idea that the radio continuum emission around young stars is dominated by shock-ionization, and this holds over several orders of magnitude of stellar luminosities (1 – 10⁵ L_⊙).

Key words. Stars: formation – Radio continuum: ISM – ISM: H II regions – ISM: jets and outflows – Techniques: high angular resolution

1. Introduction

Outflow activity is a proxy for ongoing star formation. A number of outflow studies have established a correlation between the bolometric luminosity (L_{bol}) of a star-forming region and the integrated (molecular) outflow properties, such as the mechanical force and momentum released into the ambient gas, which, at parsec scales, quantify the overall contribution of an ensemble of outflows (e.g., Arce et al. 2007; Frank et al. 2014, and references therein). This relationship holds over six orders of magnitude of L_{bol} (e.g., Beuther et al. 2002, their Fig. 4; Maud et al. 2015, their Fig. 7), and it is interpreted as evidence for a single outflow mechanism which scales with the stellar luminosity, and the outflows' motion being momentum driven. However, on scales of a few 1000 au, representative of individual young stars, there are poor statistics on outflow properties for stellar luminosities exceeding 10³ L_⊙.

For the purpose of studying the dynamical properties of the outflow emission in the vicinity of luminous young stars, we have started the “Protostellar Outflows at the Earliest Stages”

(POETS) survey. The target sample has been selected with the idea of combining the kinematic information of outflowing gas, inferred from the H₂O maser emission, with the information of ejected mass, inferred from the H II, free-free, continuum emission (e.g., Moscadelli et al. 2016; Sanna et al. 2016).

On the one hand, H₂O maser emission traces shocked gas propagating in dense regions ($n_{\text{H}_2} > 10^6 \text{ cm}^{-3}$) at velocities between 10 and 200 km s⁻¹ (e.g., Hollenbach et al. 2013): these properties make H₂O masers signposts of (proto)stellar outflows within a few 1000 au from their driving source. Maser spots, namely “cloudlets” of the order of a few au in size, are ideal test particles to measure the local three-dimensional motion of gas shocked where stellar winds and jets impact ambient gas (e.g., Torrelles et al. 2003; Goddi et al. 2006; Sanna et al. 2012; Moscadelli et al. 2013; Burns et al. 2016; Hunter et al. 2018).

On the other hand, thermal (bremsstrahlung) continuum emission, with flux densities lower than a few mJy, and spectral index values (α) at centimeter wavelengths between -0.1 and below 2, traces the ionized gas component of stellar winds and jets

(Panagia & Felli 1975; Reynolds 1986; Anglada 1996; Anglada et al. 1998). Ionization is caused by shocks around young stars with spectral types later than B, which emit negligible Lyman flux (Curiel et al. 1987, 1989). In these sources, the centimeter continuum luminosity scales with the stellar luminosity as a power law of index 0.6, approximately (Anglada 1995; Anglada et al. 2015). Extrapolating this law to young stars of spectral types B and earlier, one expects, for instance, a continuum flux of approximately 1 mJy at 8 GHz, for a B1 zero-age-main-sequence (ZAMS) star at a distance of 1 kpc from the Sun. For comparison, a homogeneous, optically thin H II region, that is excited by the Lyman photons of a B1 ZAMS star, emits a continuum flux more than two orders of magnitude higher (≈ 0.2 Jy), at the same frequency and distance. It follows that, ionized stellar winds and jets can be detected prior to the ultra-compact (UC) H II region phase, which implies typical lifetimes older than 10^4 yr (e.g., Churchwell 1999, 2002; Hoare et al. 2007).

Recently, two distinct surveys have searched for ionized stellar winds and jets in regions with bolometric luminosities typically exceeding $10^3 L_{\odot}$ (Rosero et al. 2016; Purser et al. 2016). Rosero et al. made use of the Karl G. Jansky Very Large Array (VLA) at 6 and 22 GHz to survey 58 star-forming regions at different stages of evolution. They detected ionized jet emission in about half the sample, with typical values of angular resolution and sensitivity of 0.4–0.3 arcsec and $5\text{--}10 \mu\text{Jy beam}^{-1}$, respectively. Purser et al. made use of the Australia Telescope Compact Array (ATCA) at 5, 9, 17, and 22 GHz to survey 49 star-forming regions selected from the RMS survey. They detected ionized jet emission in 26 distinct sites (12 of which are candidates), with typical values of angular resolution and sensitivity ranging between 2–0.5 arcsec and $17\text{--}106 \mu\text{Jy beam}^{-1}$, respectively. In particular, Purser et al. reported non-thermal knots in a subset of jets (10), which resemble the prototypical magnetized jet in HH 80–81 (Carrasco-González et al. 2010; Rodríguez-Kamenetzky et al. 2017).

In order to provide a homogeneous sample of stars at an early stage of evolution, we limited the sample to rich H₂O maser sites not associated with UCH II regions (where the continuum emission exceeds 10,000 au in size). Among the H₂O maser sites satisfying this requirement, we selected those targets whose distances were accurately determined by trigonometric parallax measurements, and where the maser positions are known at milli-arcsecond resolution (Reid et al. 2014). The POETS sample of 36 distinct fields, listed in Table 1, was surveyed with the VLA at 6, 15, and 22 GHz in the A- and B-array configurations. In Moscadelli et al. (2016), we presented a pilot study of 11 targets belonging to the POETS survey (hereafter, Paper I). More details about the target selection can be found in Paper I. Here, we present the full sample of radio continuum sources; a following paper will combine continuum and maser information.

In Sections 2 and 3, we summarize the observation information and explain the details of the data analysis, respectively. In Section 4, we present and discuss the overall results of the radio continuum survey. Conclusions are drawn in section 5.

2. Observations and calibration

We conducted VLA¹ observations, under program 14A-133, at C, Ku, and K bands towards 26 distinct Galactic fields associated with strong H₂O maser emission (Table 1). Towards each

¹ The National Radio Astronomy Observatory is a facility of the National Science Foundation operated under cooperative agreement by Associated Universities, Inc.

Table 1. Target fields of the POETS survey.

Field	Phase Center		$L_{\text{H}_2\text{O}}$ ($10^{-5} L_{\odot}$)
	R.A. (J2000) (h m s)	Dec. (J2000) ($^{\circ}$ ' ")	
G009.99–0.03	18:07:50.100	–20:18:56.00	0.75
G012.43–1.12	18:16:52.100	–18:41:43.00	4.98
G012.90–0.24	18:14:34.400	–17:51:52.00	0.36
G012.91–0.26	18:14:39.400	–17:52:06.00	0.05
G014.64–0.58	18:19:15.500	–16:29:45.00	0.10
G026.42+1.69	18:33:30.500	–05:01:02.00	0.31
G031.58+0.08	18:48:41.700	–01:09:59.00	0.77
G035.02+0.35	18:54:00.700	+02:01:19.00	0.63
G049.19–0.34	19:22:57.800	+14:16:10.00	9.87
G076.38–0.62	20:27:25.500	+37:22:48.00	0.24
G079.88+1.18	20:30:29.100	+41:15:54.00	0.08
G090.21+2.32	21:02:22.700	+50:03:08.00	0.03
G105.42+9.88	21:43:06.500	+66:06:55.00	0.16
G108.20+0.59	22:49:31.500	+59:55:42.00	3.61
G108.59+0.49	22:52:38.300	+60:00:52.00	0.15
G111.24–1.24	23:17:20.800	+59:28:47.00	1.06
G160.14+3.16	05:01:40.200	+47:07:19.00	0.41
G168.06+0.82	05:17:13.700	+39:22:20.00	14.32
G176.52+0.20	05:37:52.100	+32:00:04.00	0.14
G182.68–3.27	05:39:28.400	+24:56:32.00	0.41
G183.72–3.66	05:40:24.200	+23:50:55.00	1.51
G229.57+0.15	07:23:01.800	–14:41:36.00	0.71
G236.82+1.98	07:44:28.200	–20:08:30.00	0.51
G240.32+0.07	07:44:51.900	–24:07:43.00	1.24
G359.97–0.46	17:47:20.200	–29:11:59.00	1.57
Targets presented in Moscadelli et al. (2016)			
G005.88–0.39	18:00:30.306	–24:04:04.48	1.86
G011.92–0.61	18:13:58.120	–18:54:20.28	3.27
G012.68–0.18	18:13:54.744	–18:01:47.57	8.83
G016.58–0.05	18:21:09.084	–14:31:49.56	^a 4.36
G074.04–1.71	20:25:07.104	+34:49:58.58	0.25
G075.76+0.34	20:21:41.086	+37:25:29.28	0.75
G075.78+0.34	20:21:41.086	+37:25:29.28	7.98
G092.69+3.08	21:09:21.724	+52:22:37.10	2.98
G097.53+3.18	21:32:12.441	+55:53:50.61	69.72
G100.38–3.58	22:16:10.368	+52:21:34.11	1.40
G111.25–0.77	23:16:10.360	+59:55:29.53	1.36

Notes. Column 1: field name. Columns 2 and 3: phase center of the observations. Column 4: isotropic H₂O maser luminosity. For each source, this luminosity refers to the averaged luminosity measured with the VLBA in the period from March 2011 to April 2012 (from the BeSSeL Survey data). The isotropic maser luminosity was estimated with the following formula: $(L_{\text{H}_2\text{O}}/L_{\odot}) = 2.3 \cdot 10^{-8} \times (S_{\text{H}_2\text{O}} \text{ Jy km s}^{-1}) \times (D/\text{kpc})^2$, where $S_{\text{H}_2\text{O}}$ and D are, respectively, the integrated H₂O maser flux and the heliocentric distance to the H₂O maser site. ^(a) Luminosity estimated from data in Sanna et al. (2010a).

field, we observed with the A-array configuration at C and Ku bands, and with the B-array configuration at K band, in the periods March–May 2014 and February–March 2015, respectively.

For high-sensitivity continuum observations in the C, Ku, and K bands, we employed the 3-bit samplers observing dual polarization over the largest receiver bandwidth of 4, 6, and 8 GHz, respectively. At each band, we made use of the wide-band setup, tuning, respectively, 2, 3, and 4 2-GHz wide IF pairs

Table 2. Summary of VLA observations (code 14A-133).

Band	ν_{center} (GHz)	BW (GHz)	Array	On-source (min)	θ_{LAS} ($''$)	HPBW ($''$)	RMS noise ($\mu\text{Jy beam}^{-1}$)	RMS T_b (K)
C	6.0	4.0	A	15	8.9	0.33	8.0	3.0
Ku	15.0	6.0	A	10	3.6	0.13	9.0	3.0
K	22.2	8.0	B	15	7.9	0.29	11.0	0.3

Notes. Columns 1, 2, and 3: radio band, central frequency of the observations, and receiver bandwidth used. Columns 4 and 5: array configuration and on-source integration time at each band. Column 6: maximum recoverable scale of the emission at a given frequency. *The following values were derived from the VLA Exposure Calculator (v.18A).* Column 7: approximate synthesized beam size obtained with Robust weighting. Columns 8 and 9: expected thermal rms noise and corresponding brightness temperature. The rms values were estimated assuming a 15 % loss of bandwidth at each frequency.

across the receiver bandwidth. Each IF comprised 16, 128-MHz wide subbands with a channel spacing of 1 MHz. At C and K bands, we also used a narrow spectral unit of 4 MHz centered on the 6.7 GHz methanol and 22 GHz water maser lines. These bands had widths of 180 and 54 km s⁻¹ to cover the respective maser emission. In addition, they were correlated with 1664 and 128 channels to achieve sufficient velocity resolutions of 0.1 and 0.4 km s⁻¹ to spectrally resolve single maser lines. In the following, we report on the radio continuum data.

Our previous pilot observations, conducted under program 12B-044 (Moscadelli et al. 2016), have demonstrated that the free-free continuum emission, associated with the H₂O masers, has peak flux densities of a few 100 μJy at centimeter wavelengths, on average. Therefore, we integrated on each source for 10–20 minutes, in order to achieve a thermal rms noise of the order of 10 $\mu\text{Jy beam}^{-1}$, and a signal-to-noise ratio in excess of 10, typically. More details on the observational strategy can be found in Section 3.1 of Moscadelli et al. (2016). Observation information is summarized in Table 2.

Data reduction was performed within the Common Astronomy Software Applications package (CASA), making use of the VLA pipeline. Radio fluxes were calibrated with the Perley-Butler 2013 flux density scale. Additionally, we flagged each dataset based on the quality of both the amplitude and phase calibration, and performed self-calibration on those radio continuum maps which were limited in dynamic range ($10 < \text{SNR} < 50$), corresponding to source fluxes greater than a few 100 μJy .

3. Method

For each field, in Figs. 1–5 we present the radio continuum maps in the C, Ku, and K bands and analyse the radio spectral index of the continuum emission following two methods: by integrating the radio fluxes at each band and fitting the spectral slope among the bands (Sect. 3.2); by comparing the radio emission among the bands in the uv -plane directly (Sect. 3.3), making use of the multi-frequency-synthesis (MFS) deconvolution of the task *clean* of CASA (Rau & Cornwell 2011). In the following, we provide the details of our analysis.

3.1. Continuum maps

At variance with our pilot program 12B-044 (Paper I), we observed at K band with the B-array configuration instead of the A-array, so that the C- and K-band observations are sensitive to the same angular scales, covering a common range of spatial frequencies ($< 900 \text{ k}\lambda$). The observations at Ku band cover greater uv -distances in excess of 2000 $\text{k}\lambda$. Continuum maps are shown in the left panels of Figs. 1–5 for each frequency band. Imaging remarks are listed in the following:

Beam & weighting. Each field was imaged with the task *clean* of CASA interactively and with a circular restoring beam (column 4 of Table 3). The restoring beam size was set equal to the geometrical average of the major and minor axes of the clean beam size. The pixel size is a factor 0.2–0.25 of the half-power-beam-width (HPBW). By rule of thumb, the C- and K-band maps were produced with a common Briggs robustness parameter of 0.5, to simultaneously optimize side-lobes suppression and sensitivity; the Ku-band maps were produced with natural weightings to enhance the sensitivity in the shortest baselines. For faint sources with peak brightness below 7σ , we applied natural weightings without distinction. The beam size ranges from a minimum of 0 $''$.110, at Ku band, to a maximum 0 $''$.481, at C band.

UV-range. At the bottom of each plot, we indicate with “UV-CUT” or “TAPER” whether a lower limit to the uv -range or tapering were used for cleaning, respectively. At each frequency, the targets in our sample are more compact than the largest angular size (θ_{LAS}) which can be imaged with the A- and B-array configurations (Table 2). On the other hand, 5 fields in our sample exhibit extended bright continuum emission (other than the targets) which cannot be recovered without shorter baselines. Since this emission adds to the image residuals, and limits the image sensitivity, we cleaned those fields by setting a lower cut to the uv -plane. A lower cut of 100 $\text{k}\lambda$ corresponds to filter out emission more extended than 2 $''$. Details are given in the footnotes to Table 3.

Field-of-view. In Figs. 1–5, we limited the field-of-view so as to include the radio continuum sources closest to the H₂O maser emission detected in the field. For the brightest maser spots ($\geq 0.5 \text{ Jy beam}^{-1}$), absolute positions can be obtained from the Bar and Spiral Structure Legacy (BeSSeL) website at http://bessel.vlbi-astrometry.org/first_epoch (Reid et al. 2014). In each plot, we draw a scale bar to quantify the linear size of the field; the linear size was computed from the distance values reported in Table 1 of Paper I. Field-of-views range from a minimum of 650 au (Fig. 2) to a maximum of 9000 au (Fig. 1).

For each field, we superpose, where available, the C-band emission in black contours (and gray tones), the Ku-band emission in red contours, and the K-band emission in blue contours. Map contours are listed at the bottom of each plot and are scaled at multiples of the 1σ rms (column 5 of Table 3). The rms noise was estimated with the task *imstat* of CASA, across a region without continuum emission. Alternatively, we indicate whether the field was not observed at a given frequency band, or the emission was not detected above a 3–5 σ level.

When multiple radio continuum peaks exceeding 5σ are detected (e.g., Fig. 1), individual peaks are labeled with numbers increasing with decreasing brightness. For each peak or

“component” in Table 3, we report the maximum pixel position (columns 6–7), the maximum pixel value (column 8), and the integrated flux (column 10) obtained with the task *imstat* of CASA. Values of integrated flux are measured in images produced with a common uv -coverage among the bands (see Sect. 3.2). The flux density of single components was computed within the 3σ contour at each band. Blended sources were detected in 2 fields (Figs. 1 and 3), and their flux densities were computed within squared boxes centered on each peak.

In column 9 of Table 3, we assign a grade to each source depending on the compactness of the emission. We fitted the continuum emission within the 3σ contour with a two-dimensional (elliptical) Gaussian (task *imfit* of CASA), and classified the source size as follows: the source is compact (“C”) if its deconvolved size is smaller than half the beam size; the source is slightly resolved (“SR”) if its deconvolved size is smaller than the beam and larger than half the beam size; the source is resolved (“R”) if its deconvolved size is larger than the beam size.

3.2. Spectral energy distributions

In Figs. 1–5, we show the results of the spectral index analysis based on the integrated fluxes at each band (SED), under the assumption that: $S_{\nu_1}/S_{\nu_0} = (\nu_1/\nu_0)^\alpha$. As a caveat to the spectral index analysis, we assume there was no significant source variability during the one-year interval between the A- and B-array configurations. Similar to Paper I, we measured the continuum spectral index following four steps:

1. First, we constrained a common uv -range among the radio bands of 40–800 k λ , and imaged each band separately with the same round beam (0'30) and pixel size (0'06). Higher values of the minimum uv -distance were used for 4 fields (see Sect. 3.1). On top of each plot, we specify the range of uv -distances selected for a given field.
2. These maps were used to select a polygon around the source which encloses the continuum emission; these polygons typically correspond to the 3σ contours. For instance, sources detected at C, Ku, and K bands define three distinct polygons. At a given frequency, we estimated the integrated flux as the averaged flux over the three polygons. The uncertainty of the averaged flux was estimated as the dispersion of the mean, and was summed in quadrature with a 10% error in the absolute flux scale. This method takes into account that, due to small position shifts among the C-, Ku-, and K-band maps ($\leq 0'1$), the same polygon does not trace the same region at different frequencies.
3. We used the averaged fluxes and their uncertainties to compute the continuum spectral index with a linear regression fit, where: $\log_{10}(S_\nu) = \alpha \cdot \log_{10}(\nu) + \text{const}$. For sources only detected at K band, we provide a lower limit to the spectral index, by fitting a straight line to the K-band flux and the upper limit of the Ku-band flux.
4. We plot the averaged fluxes at the C, Ku, and K bands (Fig. 1–5); each frequency is identified with the same color used for the continuum maps. In each plot, we draw the spectral index values (and uncertainties) of the different band combinations, as well as the spectral index among the three bands where available.

In column 11 of Table 3, the best-fitting value of the spectral index is given for each source.

3.3. Spectral index maps

In Figs. 1–5, we provide an alternative analysis of the continuum spectral index based on the MFS cleaning (Rau & Cornwell 2011, and references therein), under the assumption that: $I_{\nu_1}/I_{\nu_0} = (\nu_1/\nu_0)^\alpha$. The task *clean* of CASA was run with parameter *nterm* = 2, which expands the observed brightness distribution taking into account the first two terms of a Taylor series: $I_\nu = I_{\nu_0} + \alpha \cdot I_{\nu_0} \cdot (\nu - \nu_0)$. This procedure produces a set of Taylor-coefficient images (Sects. 2.2 and 2.7 of Rau & Cornwell 2011): the first coefficient of the Taylor expansion defines the average brightness distribution (in CASA, map extension “.t0”); the spectral index map is derived from the second coefficient (in CASA, map extension “.alpha”), which is the product of the average brightness times the local spectral index value. The MFS algorithm compares observed and modeled visibilities in the uv -plane, providing information on the spatial distribution of the spectral index value, as opposed to the average spectral index inferred in Sect. 3.2. Hereafter, we refer to this method as the “ α -map”.

Since the accuracy of the spectral index calculation depends on the SNR of the brightness distribution, the following constraints apply:

1. α -maps were only processed for those sources where the continuum emission exceeds 7σ at each band;
2. α -maps are only displayed where these two conditions hold: the average map exceeds 7σ , and the uncertainty of α estimated by the algorithm is less than 0.2–0.3 (map extension “.alpha.error”).

For each source which satisfies the first requirement, we cleaned the datasets available all together with a Briggs robustness parameter of 0.5. In Figs. 1–5, each α -map shows the average brightness map in contours and the spectral index map in colors, according to the right-hand wedge. In each plot, we also specify the center frequency of the average brightness map, and the uncertainty on α , which increases from the brightness peak, where $\Delta\alpha < 0.1$ typically, to the outer iso-contour, where $\Delta\alpha = 0.2$ or 0.3.

In Appendix A, we show that small position shifts, between maps at different frequency bands, produce systematic variations in the spectral index maps. Since these position shifts are of the same order of the calibration uncertainties, one has to exert caution when interpreting spectral index gradients.

4. Results and discussion

In this section, we firstly discuss the details of four examples of radio continuum emission (Figs. 1–4), which provide the background to interpret the entire sample of sources (Fig. 5). We then comment on the nature of the radio continuum emission by comparing the radio luminosity of our sample with both the H₂O maser and bolometric luminosities.

In the following, if the radio continuum SED is well reproduced with a linear spectral slope, we will use the terms (ionized) *stellar wind* and *thermal jet* to distinguish between unresolved and resolved/elongated emission, respectively. In column 12 of Table 3, we provide a classification for the entire sample of sources, which split as follows: 15 stellar winds, 8 thermal jets, 2 H II regions, and 7 sources detected at one frequency only (and not classified).

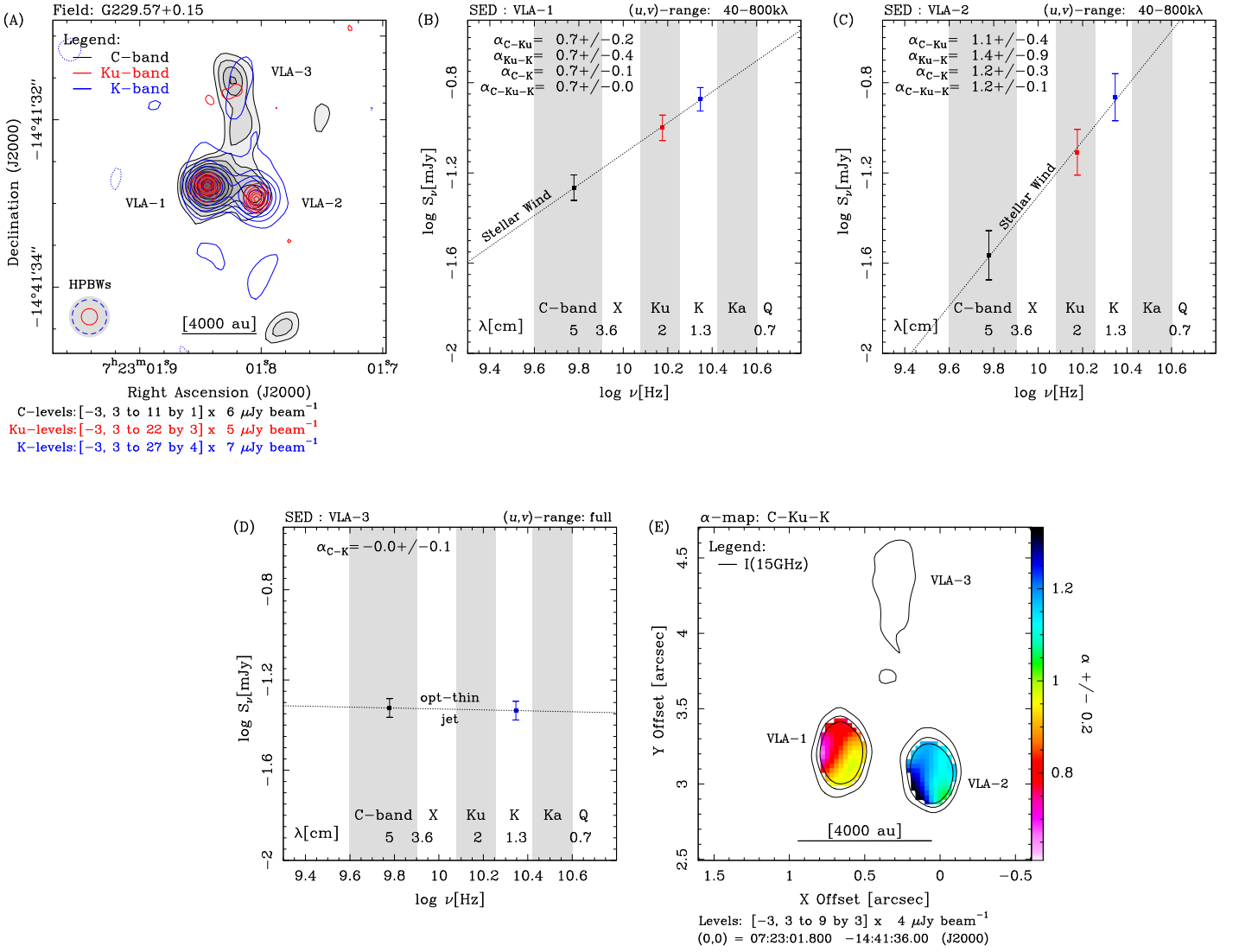


Fig. 1. Example of stellar wind emission from a double system: H₂O maser site G229.57+0.15 (Sect. 4.1). **Panel A:** superposition of the VLA maps for the C- (grey-scale/black contours), Ku- (red), and K-band (blue) emission (Sect. 3.1). Contour levels, at multiples of the 1σ rms, are indicated in the footnote. Synthesized beams for each band are shown in the bottom left corner. A scale bar in units of au is drawn near the bottom axis. Three distinct continuum sources are identified and labeled VLA-1, VLA-2, and VLA-3, from the brightest to the faintest. **Panels B-D:** spectral energy distribution for the three sources identified in panel A separately (Sect. 3.2). Each plot shows the logarithm of the integrated flux (in mJy) as a function of the logarithm of the observed frequency (in Hz). Different frequency bands are labeled near the bottom axis together with the reference wavelength; grey shades mark the boundary of each band. For each band combination, the linear spectral index value (α) and its uncertainty are specified in the upper left corner. The common range of of uv -distances (e.g., 40–800 k λ in panel B, and full uv -range in panel D), used to compute the integrated fluxes among the bands, is indicated in the upper right. **Panel E:** color map of the linear spectral index (α) computed with the multi-frequency-synthesis algorithm of the task *clean* of CASA (Sect. 3.3). Frequency bands used to fit the spectral index are listed on top; spectral index values are quantified by the right-hand wedge. The uncertainty on α is indicated in the wedge label; this value is an upper limit which holds at the 7σ contour of the average brightness map (black contours). Contour levels of the average brightness map, at multiples of the 1σ rms, are indicated in the footnote; the central frequency (ν_0) of the average brightness map is specified in the legend. The absolute coordinates of (0,0) offset are indicated in the footnote (see Table 1). Radio continuum components and the scale bar as in panel A.

4.1. Example 1: compact stellar winds from a double system

In Fig. 1, we present an example of stellar wind sources towards the H₂O maser site G229.57+0.15. In panel A, we plot the brightness distribution of the continuum emission detected in the three observed bands. These maps show two compact sources, labeled VLA-1 and VLA-2, which are aligned along the east-west direction, and a region of extended (resolved) emission, labeled VLA-3, which extends northwards of VLA-1 and VLA-2. The radio continuum peaks of VLA-1 and VLA-2 are separated by about 2800 au (Table 3). These maps were produced with natural weightings, to retrieve the extended flux associated

with VLA-3, and have approximately the same rms noise of 5–7 μ Jy beam⁻¹.

Radio continuum components VLA-1 and VLA-2 have comparable brightness at K band of 170 μ Jy beam⁻¹, but the peak of VLA-2 is about half that of VLA-1 at C-band (Table 3). This difference determines a much steeper gradient in the SED of VLA-2 with respect to that of VLA-1, which is evident by comparing panels B and C of Fig. 1. In both panels, the integrated fluxes computed at each frequency are strictly aligned, and define a linear gradient (α) between the C, Ku, and K bands of 0.68 ± 0.02 and 1.2 ± 0.1 , for the VLA-1 and VLA-2 sources

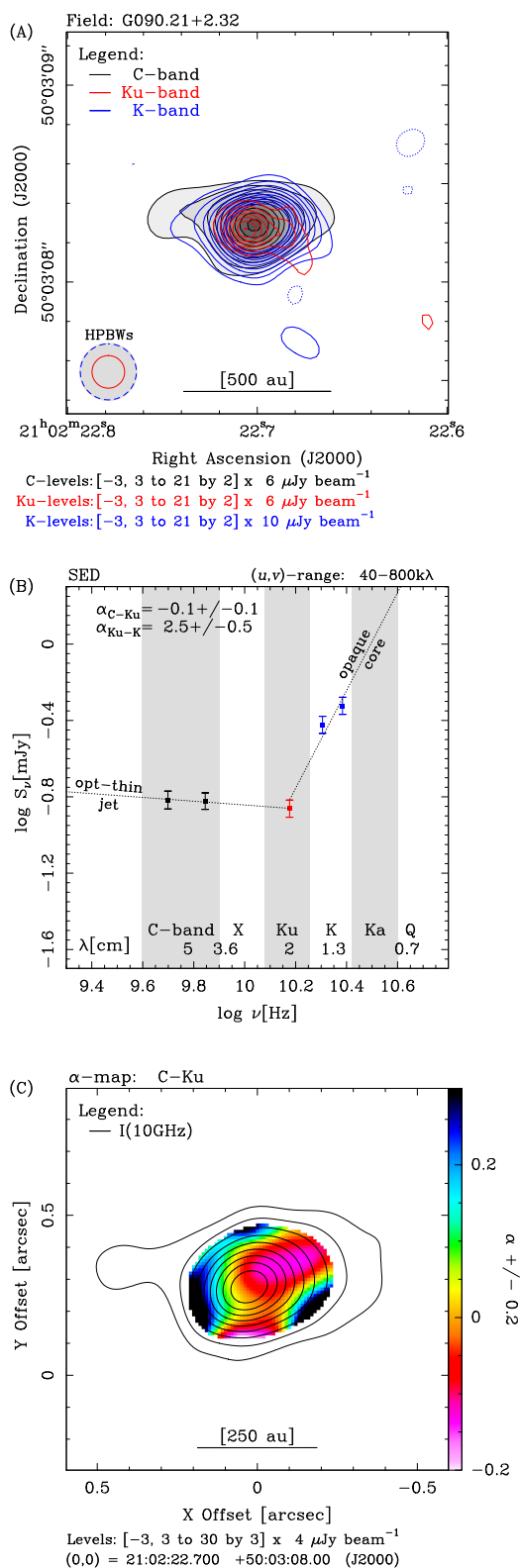


Fig. 2. Example of optically-thin thermal jet emission: H_2O maser site G090.21+2.32 (Sect. 4.2). Labels and symbols as in Fig. 1. In panel B, we have divided the C and K bands in two sub-bands, in order to show that the spectral index within each band is consistent with the spectral index interpolated to the Ku-band frequency. The spectral energy distribution shows a region of optically thin (resolved) emission below 15 GHz, and a region of optically thick (compact) emission above 15 GHz. The spectral index map of panel C was computed within the (linear) range of optically thin emission (C and Ku bands only).

respectively. The higher flux uncertainties of VLA–2, with respect to VLA–1, are due to the larger difference between the fluxes integrated within the C-, Ku-, and K-band boxes. These boxes coincide with the 3σ contours everywhere except between VLA–1 and VLA–2, where we drew a clear cut along the north-south direction to separate the emission. The spectral index values of VLA–1 and VLA–2 are consistent with the radio continuum emission being produced by thermal bremsstrahlung from a stellar wind.

At variance with sources VLA–1 and VLA–2, source VLA–3 is resolved out at the Ku band, and, to derive the continuum spectral index in this region, we made use of the C and K bands only (panel D). Since the C and K bands observations are sensitive to the same spatial scales, we did not limit the uv -range to compute the integrated fluxes, and used a squared box which encloses the emission between a declination of $-14:41:32.03$ and $-14:41:31.17$. The spectral index value of VLA–3 is of 0.0 ± 0.1 , and, taking into account the spatial morphology of the radio continuum emission, it is consistent with thermal bremsstrahlung from an optically thin radio jet. This emission might be associated either with VLA–1 or VLA–2.

In panel E, we plot the spectral index map determined from the combination of the C-, Ku-, and K-band datasets; this map is **referred** to the central frequency of the Ku band (15 GHz). Only sources VLA–1 and VLA–2 have sufficiently high SNR ($> 7\sigma$) to compute the spectral index in the uv -domain with high accuracy. The color scale of panel E shows that the spectral index of VLA–1 ranges from 0.65 to 0.95, encompassing the average value determined in panel B. The extremes of the alpha range coincide with the 7σ contour of the average brightness map (black contours), where the uncertainty on α increases to ± 0.2 . Similarly, the spectral index map of VLA–2 converges, towards the brightness peak, on the average value determined in panel C; the spectral index varies over an interval 1.0–1.3 of about 1σ .

Notably, sources VLA–1 and VLA–2 make the case for two nearby (unresolved) stellar winds with sharply different spectral indexes. Following Reynolds (1986), the higher spectral index value of VLA–2 may be interpreted as the radio continuum opacity changing more rapidly in VLA–2 than in VLA–1. We make use of eq. 15 of Reynolds (1986), which quantifies the spectral index of a radio jet as a function of its geometry (ϵ), temperature (q_T), and optical depth (q_r) variations across the flow. We assume that the two flows are either spherical or conical ($\epsilon = 1$), and since both sources are unresolved at the beam scale, we take an upper limit to the source size of $0''.206$ at K band, corresponding to 930 au at a distance of 4.52 kpc. We also assume that the ionized gas is approximately isothermal within a radius of 500 au from the central source ($q_T = 0$). Under these conditions, eq. 15 of Reynolds (1986) predicts that: $(\alpha_1 - \alpha_2)/4.2 = (1/q_{r1}) - (1/q_{r2}) = -0.12$, where q_{r1} and q_{r2} are negative parameters, and the subscripts 1 and 2 are relative to sources VLA–1 and VLA–2, respectively. This calculation implies that the absolute value of q_{r1} is smaller than that of q_{r2} .

4.2. Example 2: optically-thin thermal jet emission and opaque core

In Fig. 2, we present an example of radio thermal jet source towards the H_2O maser site G090.21+2.32. This source has the lowest bolometric luminosity in our sample ($27 L_{\odot}$). The radio continuum maps show that the emission is elongated in the east-west direction (panel A). At the C and Ku bands (4–18 GHz), the continuum emission is resolved at a scale of $0''.292$ and $0''.166$, respectively; at the K band (18–26 GHz), the continuum

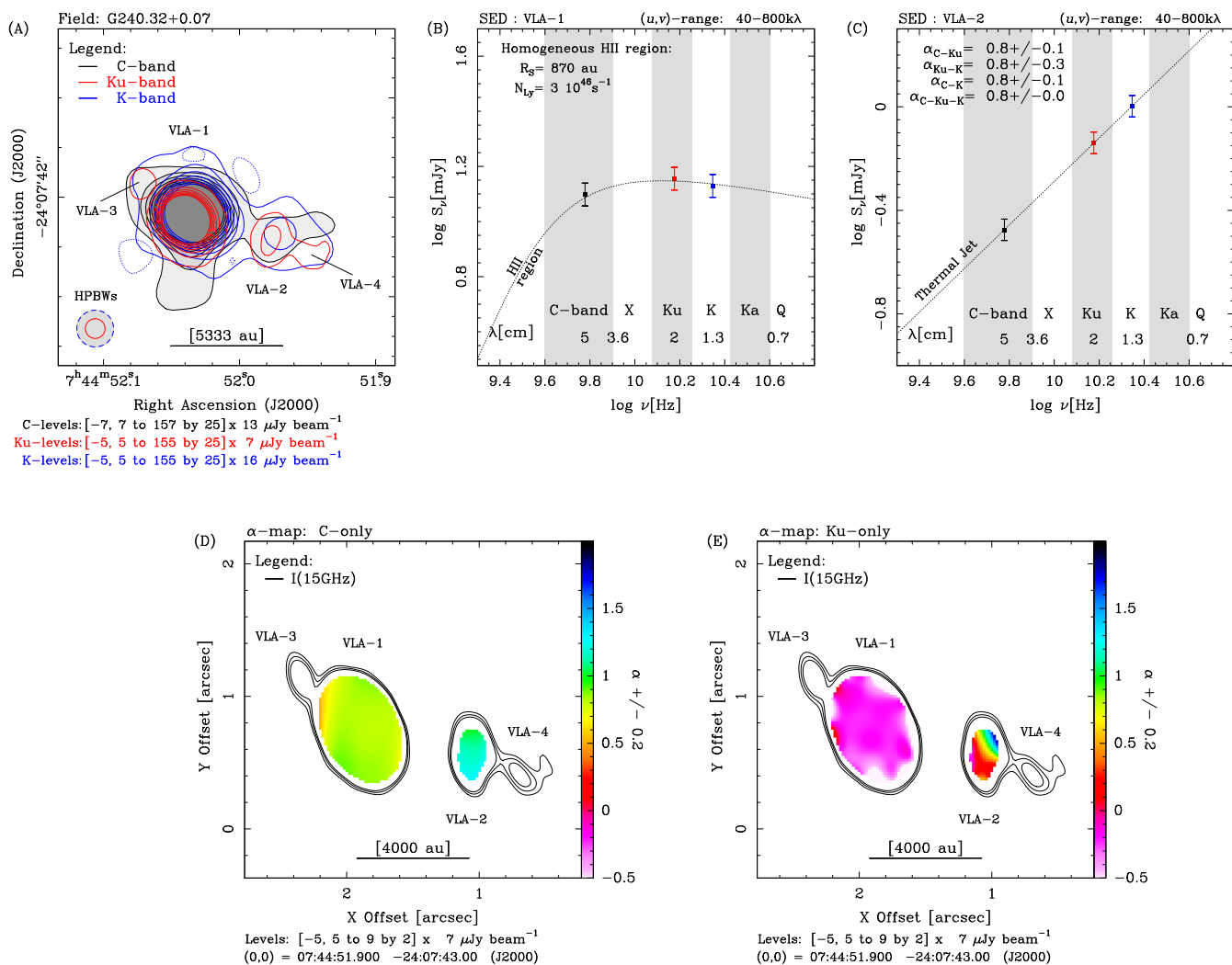


Fig. 3. Example of radio thermal jet (VLA-2) near to a HCH II region (VLA-1): H₂O maser site G240.32+0.07 (Sect. 4.3). Labels and symbols as in Fig. 1. The spectral energy distribution of source VLA-1 was fitted with a model of homogeneous H II region (panel B), with Strömgen radius of 870 au and number of Lyman photons of $3 \times 10^{46} \text{ s}^{-1}$. This model accurately reproduces the observed fluxes at each band. Thanks to the high signal-to-noise ratio, in panels D and E we can determine the spectral index maps of the C and Ku bands, separately, with an uncertainty better than ± 0.2 . The average brightness map (contours) is that of the Ku band in both panels D and E, for comparison. The spectral index maps trace the turn-over of the continuum spectrum for source VLA-1, from $\alpha = 1.0$ –6.0, between 4 and 8 GHz (panel D), to $\alpha = -0.1$, above 15 GHz (panel E).

emission has a deconvolved size of the order of half the beam ($0''.140$). At a distance of 670 pc, the source size corresponds to about 90 au in the higher frequency range, and exceeds 200 au in the lower frequency range.

The flux density at C band is comparable to that at the Ku band, which is almost three times less than the flux recovered at K band (Table 3). To verify that the difference between the Ku- and K-band fluxes does not depend on the calibration, we divided both the C and K bands in two sub-bands, each one equal to half the bandwidth, and imaged each sub-band separately. The integrated fluxes derived from each sub-band are plotted in panel B of Fig. 2. In this plot, we show that the spectral index fitted between the C and Ku bands reproduces the spectral slope determined within the C band only; similarly, the spectral slope within the K band only is consistent with that between the Ku and K bands. The spectral index values derived between the C and Ku bands (-0.1 ± 0.1), and between the Ku and K bands (2.5 ± 0.5), are consistent, respectively, with thermal jet emission which is optically thin for frequencies below 15 GHz, and with a compact core which is optically thick for frequencies above 15 GHz. This

scenario closely resembles that predicted by Reynolds (1986, e.g., their Fig. 2).

In panel C, we plot the spectral index map determined from the combination of the C- and Ku-band datasets; this map is referred to the central frequency between the C and Ku bands (10 GHz). The spectral index map ranges from -0.2 to 0.3 ; at these extremes, corresponding to the outer iso-contours, the uncertainty increases to ± 0.2 , and decreases below ± 0.1 at the brightness peak. This range of spectral index values is consistent with the average spectral index derived in panel B, within 1σ . Spectral index variations observed in panel C are likely an effect of the MFS deconvolution algorithm, produced by combining different Gaussian distributions at distinct frequency bands (see Appendix A).

4.3. Example 3: a thermal jet near to a HCH II region

In Fig. 3, we present an example of thermal jet near to a hyper-compact (HC) H II region, towards the H₂O maser site G240.32+0.07. In panel A, the radio continuum emission is

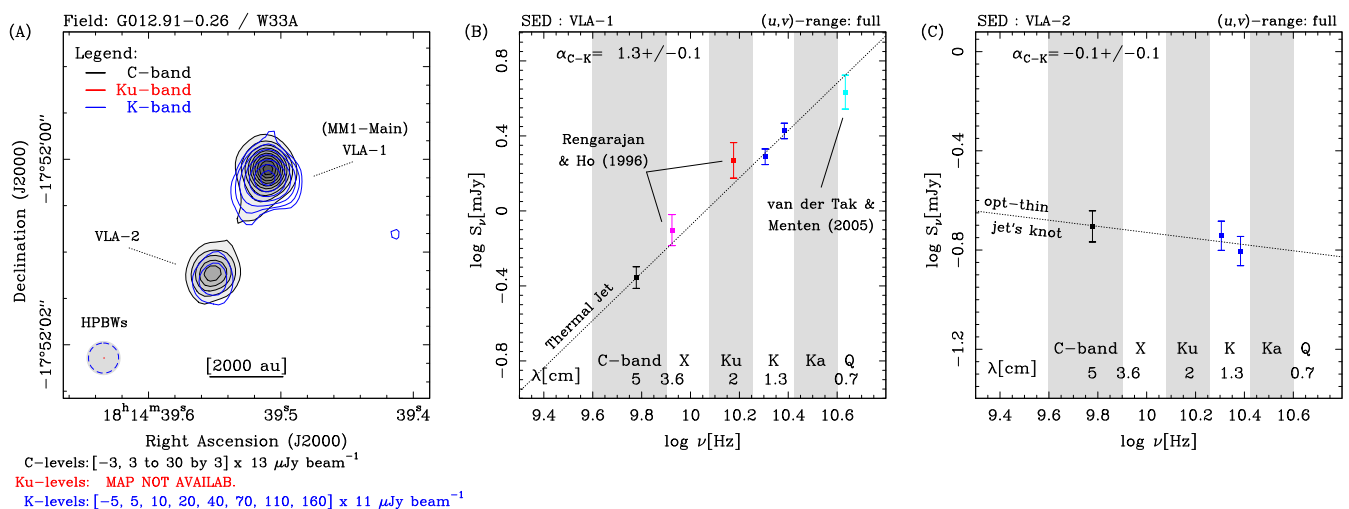


Fig. 4. Example of radio thermal jet (VLA-1) with nearby knot (VLA-2): H₂O maser site G012.91-0.26 or W33A (Sect. 4.4). Labels and symbols as in Fig. 1. Two radio continuum sources are detected at both C and K bands along a position angle of approximately 152° (panel A): the brightest emission coincides in position with the brightest millimeter source in the dusty core MM1. In panels B and C, we have fitted the spectral index of sources VLA-1 and VLA-2 with the measured fluxes at C and K bands, after dividing the K-band observations in two sub-bands, each spanning 4 GHz. In panel B, fluxes reported in the literature at X (pink), Ku (red), and Q (cyan) bands are consistent with a single linear slope, from 4 to 43 GHz. The radio continuum emission associated with W33A-MM1 can be interpreted as a thermal jet, whose components VLA-1 and VLA-2 mark, respectively, the ionized gas closest to the driving source, namely MM1-main, and a knot of shocked gas along the jet direction.

dominated by two components, labeled VLA-1 and VLA-2, which are separated by about 4300 au along the northeast-southwest direction. The peak brightness of component VLA-1 is more than 10 times higher than that of VLA-2 at each frequency, and both components have a size comparable to that of the beam (Table 3). Because of the limited uv -coverage, we performed self calibration at each band, in order to improve on the dynamic range of the maps, which exceeds a factor of 100. At Ku-band, two additional peaks are distinctly resolved to the north-east and south-west of VLA-1 and VLA-2, respectively, and have been labeled VLA-3 and VLA-4. Component VLA-3 is about 50 times less intense than VLA-1, and VLA-4 is about 6 times less intense than VLA-2 (Table 3). Because of the larger beam size, at the C and K bands VLA-3 and VLA-4 are heavily blended with, respectively, VLA-1 and VLA-2, and we do not discuss them further².

In panel B, we show that the integrated fluxes of source VLA-1 do not fit a straight line with positive slope, but can be reproduced by a model of homogeneous H II region with constant density and temperature. We fix the electron temperature of the H II region to 10⁴ K, taking into account the lower limit to the brightness temperature of 3000 K at Ku band (optically thin regime). The continuum spectrum in panel B is produced by a number of Lyman photons (N_{Ly}) of $3 \times 10^{46} \text{ s}^{-1}$ and Strömgren radius (R_S) of 870 au, corresponding to an angular size of 0'370 at a distance of 4.72 kpc (i.e., the beam size). The H II region has an electron density (n_e) of $1.2 \times 10^5 \text{ cm}^{-3}$ and emission measure (EM) of $1.2 \times 10^8 \text{ pc cm}^{-6}$. The radio continuum emission is strong enough to allow obtaining individual spectral index maps of the C and Ku bands separately (panels D and E). These maps show that the spectral index values within the C and Ku bands are in excellent agreement with the continuum spectrum of the H II region, confirming that the spectral slope is inverted between 4 and 18 GHz from positive to negative values. The number of Ly-

man photons, required to excite the HCH II region, corresponds to that emitted by a zero-age-main-sequence star of spectral type between B1-B0.5 (e.g., Thompson 1984). This star dominates the bolometric luminosity of the region of $10^{3.9} L_\odot$ (Table 1 of Paper I).

In panel C, we show that the integrated fluxes of source VLA-2 fit a straight line with angular coefficient (α) of 0.84; this averaged spectral index is constrained within a small uncertainty of ± 0.03 . The radio continuum emission from VLA-2 is consistent with thermal bremsstrahlung from a radio jet, which is elongated in the southeast-northwest direction. On the other hand, the spectral index maps of the C and Ku bands encompass a wide range of (positive) spectral index values. At C band (panel D), α ranges between 1.0 and 1.3; this range is consistent with a single value within 1σ . At Ku band (panel E), α ranges between 0 and 1.5; this range exceeds the largest uncertainty on α (± 0.2) and increases regularly from the southeast to the northwest.

According to eq. 15 of Reynolds (1986), changes of α with position might be due to changes of the flow geometry (ϵ), and irregular changes of the temperature (q_T) and optical depth (q_τ) across the flow. Practical examples are, respectively, a wide-angle wind which collimates at large radii from the star, a sudden drop of temperature away from the heating source, and the optical depth which increases towards the receding (red-shifted) lobe of the outflow and decreases towards the approaching (blue-shifted) lobe. The first two examples would produce, on the α -map, a symmetric gradient with respect to the central source, whereas the third example would produce a continuous change of α across the flow, from the red-shifted lobe (higher α) to the blue-shifted lobe (lower α).

Assuming that the source exciting VLA-2 is at the center of the radio continuum emission, a change in the optical depth, between the red-shifted jet lobe (to the northwest) and the blue-shifted jet lobe (to the southeast), would explain the regular gradient of α . This interpretation is consistent with the geometry of the molecular outflow detected in the region by Qiu et al.

² Flux densities of components VLA-1 and VLA-2 were computed within squared boxes centered on each peak. The box size was set so as to minimize the contribution of sources VLA-3 and VLA-4, based on the Ku-band map.

(2009). In Appendix A, we generally comment on the variations observed in the spectral index maps.

4.4. Example 4: a thermal jet with nearby knot – W33A

As a last example, we detail on the case of W33A, for which X-, Ku-, and Q-band data are available from the literature. We targeted this field at both C and K bands; C-band observations were conducted under program 12B-044 and are described in Paper I. We have detected two radio continuum components (Fig. 4 A), labeled VLA–1 and VLA–2, which are separated by about 3300 au along the northwest-southeast direction. Source VLA–1 coincides in position with the brightest peak of the main dust condensation MM1 (e.g., Fig. 1 of Galván-Madrid et al. 2010), and was previously detected at 3.6 cm, 2 cm, and 7 mm by Rengarajan & Ho (1996) and van der Tak & Menten (2005). Source VLA–2, which is an order of magnitude less bright than VLA–1 at 1 cm, has never been detected before, and does not coincide with millimeter dust emission (e.g., Fig. 1 of Galván-Madrid et al. 2010, and Fig. 1 of Maud et al. 2017).

In panel B, we make use of data from the literature to show that the flux density of source VLA–1 exhibits a steady increase over a wide interval of frequencies, from 4 to 43 GHz. Since we did not observe this field at Ku band, we divided the K-band data in two sub-bands, each one equal to half the bandwidth, in order to prove that the spectral slope between the C and K bands is preserved within the K-band itself. The C-band integrated flux and the two K-band integrated fluxes fit a linear spectral slope of 1.26 ± 0.06 , consistent with thermal bremsstrahlung emission from a stellar wind or jet. The spectral index of source VLA–1 is higher than 1 to a 5σ confidence: this result points to acceleration or recombination in the flow, according to Reynolds (1986). In panel B, we also plot the flux densities measured at X (0.79 mJy) and Ku (1.86 mJy) bands from Table 2 of Rengarajan & Ho (1996), and the Q-band flux density (4.3 mJy) from Table 1 of van der Tak & Menten (2005). We account for a 20% uncertainty of the absolute flux scale at X, Ku, and Q bands; these observations were conducted on April 1990, February 1984, and September 2001, respectively.

In panel C, we show that the spectral index of radio component VLA–2 (-0.12 ± 0.08) is that of optically-thin continuum emission. For the spectral index analysis, the K-band data were split in two sub-bands as in panel B. Radio thermal jet emission is expected to become totally transparent ($S \propto \nu^{-0.1}$) away from the driving source (Reynolds 1986). Combining this information with the spatial information of the outflow emission from MM1-main, we interpret source VLA–2 as a knot of the radio jet. The near-infrared and molecular outflow emission driven by MM1-main is elongated at a position angle (east of north) between 133° and 145° (de Wit et al. 2010; Davies et al. 2010; Galván-Madrid et al. 2010). Accordingly, radio components VLA–1 and VLA–2 are aligned along a position angle of 152° , measured between the K-band peaks.

4.5. L_{rad} versus $L_{\text{H}_2\text{O}}$ and L_{bol}

In Fig. 6, we study the properties of the radio continuum emission for sources associated with H₂O masers. We plot the radio luminosity of the POETS sample (red diamonds) as a function of the isotropic H₂O maser luminosity (Fig. 6 A), and of the bolometric luminosity of the young stars (Fig. 6 B). For a direct comparison with previous studies, we have interpolated the radio luminosities to 8 GHz, taking into account, for each source, the

spectral index calculations performed in Sect. 3.2 (cf. Anglada 1995; Purser et al. 2016; Tanaka et al. 2016). On the one hand, the POETS sample was selected so that absolute positions of the H₂O masers are known with uncertainties of a few milli-arcseconds, allowing us to associate the maser emission with the radio continuum sources without ambiguity. On the other hand, six radio continuum sources are found in fields with high multiplicity: since the bolometric luminosity³ of these sources cannot be established, they are not plotted in Fig. 6 B. These fields are indicated in Table 3, and add to the two fields excluded in Moscadelli et al. (2016, their Fig. 13). Additional notes are reported in Table 3.

In order to better sample the range of H₂O and bolometric luminosities, we complement the analysis by including a number of radio continuum sources from the literature, which are also associated with H₂O masers. We made use of the sample by Furuya et al. (2003, green circles) to cover the lowest H₂O maser luminosities (Fig. 6 A), which are also associated with the less-luminous young stars (Fig. 6 B). Furuya et al. monitored the H₂O maser emission with the Nobeyama 45 m telescope towards a sample of young stars, with luminosities of the order of $10 L_\odot$ and distances within a few 100 pc, typically. Among their sample, we have selected those sources associated with radio continuum emission, either at 6 or 3.5 cm (their Table 4), and whose H₂O maser emission was detected at three or more epochs (15 sources in total). In Fig. 6, we plot the averaged H₂O maser luminosity from Table 2 of Furuya et al. (2003, corrected for the erratum), and computed the continuum flux at 8 GHz assuming a standard spectral index of 0.6.

We have further included in our analysis seven sources with bolometric luminosities in excess of $10^4 L_\odot$ (cyan circles in Fig. 6). These sources are associated with prototypical radio jets and H₂O masers, whose proper motions have been studied by our group with the Very Long Baseline Array (VLBA) in the recent years. Distance measurements, for all sources but HH 80-81, were obtained by maser trigonometric parallaxes. In Table 4, for each source we have listed the H₂O maser luminosity, computed from our previous measurements, and the continuum luminosity at 8 GHz, computed from the closest continuum fluxes and spectral index information available in the literature.

In panel A of Fig. 6, we show that the radio continuum and H₂O maser luminosities are related each other, and the data points are distributed along a line with a correlation coefficient (r) of 0.85. The dotted bold line draws the best fit to the sample distribution, obtained by minimizing a linear relation between the logarithms of the radio and H₂O maser luminosities, $\log_{10}(L_{8\text{GHz}}) = p \cdot \log_{10}(L_{\text{H}_2\text{O}}) + q$. Values of p and q , with their uncertainties, are reported in the plot. The lowest and the highest data points in the distribution bias the linear fit to a lower p -value of 0.69 ± 0.06 ; these two points were excluded for the final best fit.

In panel B of Fig. 6, we plot the same radio continuum luminosities but with respect to the bolometric luminosities of each source. The solid line draws the radio luminosity expected from an optically thin H II region based on the ionizing photons of ZAMS stellar models by Thompson (1984). In comparison with panel A, the data points also show a strong linear correlation (0.91) but with a less steep slope. The dotted bold line draws

³ Bolometric luminosities have been measured with the *Herschel* Hi-GAL fluxes for 60% of the POETS sample, and probe angular scales of less than $30''$. For the remaining fields, bolometric luminosities have been estimated on the basis of archival mid-infrared (WISE and MSX) and far-infrared (IRAS) fluxes (Table 1 of Moscadelli et al. 2016).

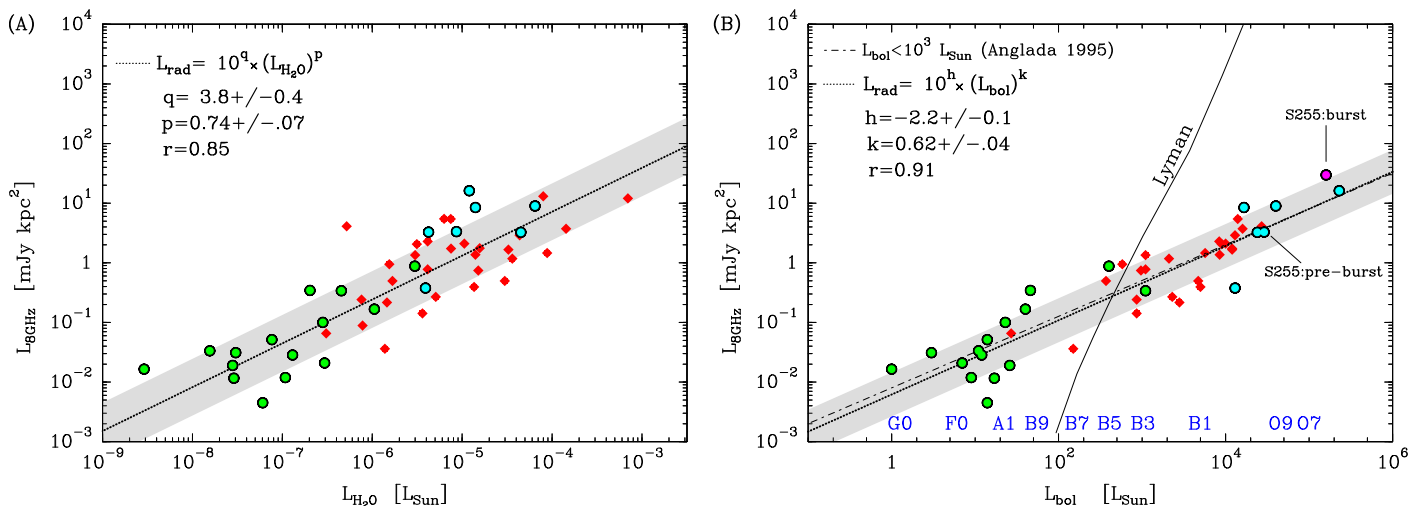


Fig. 6. Dependence of the radio luminosity of the POETS sample on the H₂O maser (left) and bolometric (right) luminosities (Sect. 4.5). Radio continuum luminosities have been normalized to 8 GHz for comparison with previous works, and a logarithmic scale is used. **Panel A:** Red diamonds mark the POETS sample (Table 1); cyan circles mark additional H₂O maser sites associated with luminous, prototypical, radio thermal jets (Table 4); green circles mark low-luminosity H₂O maser sites (from Furuya et al. 2003). The dotted bold line traces the χ^2 fit to the sample distribution; the grey shadow marks the dispersion (1 σ) about the best fit. The parameters and uncertainties of the best fit, q and p , are reported in the upper left, together with the linear correlation coefficient of the distribution (r). **Panel B:** Same symbols as in panel A. The parameters of the best fit, h and k , are to be compared with, e.g.: Anglada et al. (2015); Purser et al. (2016). The best fit to the low-mass radio jet luminosities is drawn with a dashed-dotted line (from Anglada 1995). The solid line traces the ionized flux expected from the Lyman continuum of ZAMS stars earlier than B8 (see Sect. 4.5). For ZAMS stars, spectral types, corresponding to a given luminosity, are indicated in blue near the lower axis (from Thompson 1984). The pink circle marks the bolometric and radio luminosities of source S255 NIRS3 during its recent accretion burst, for comparison (Caratti o Garatti et al. 2017; Cesaroni et al. 2018).

the best fit to the sample distribution similar to panel A, and the best-fit parameters are reported in the plot with their uncertainties. We explicitly note that, including or not the topmost (cyan) data point, corresponding to source AFGL 2591, does not change the fitting results. Also, source S255 NIRS3 has been recently discovered to undergo an accretion burst (Caratti o Garatti et al. 2017), which triggered a progressive increase of radio thermal jet emission (Cesaroni et al. 2018). In panel B, we plot the position of source S255 NIRS3 before and after the accretion burst, showing that the radio and bolometric luminosities agree with the linear relation at different times (the data point of the burst was not used in the fitting).

The power-law dependence between the radio and bolometric luminosities of young stars has been previously explored by other authors (Anglada 1995; Hoare & Franco 2007; Purser et al. 2016; Tanaka et al. 2016). The (extended) sample of H₂O maser sources fits a power-law of 0.62 ± 0.04 (Fig. 6 B), in agreement with the fit by Purser et al. (2016, $k = 0.64 \pm 0.04$), who compiled a recent sample of thermal jets from the literature (their Fig. 2). The advantage of the H₂O maser sample is twofold: radio continuum sources have been selected on the basis of a common signpost, namely the H₂O maser emission, providing a homogeneous sample; the H₂O maser sources uniformly sample the range of bolometric luminosities. In particular, the POETS sources are under-luminous with respect to the radio luminosity expected from the Lyman continuum of ZAMS stars (for spectral types earlier than B6). This evidence is suggestive that the young stars exciting the continuum emission are at an early stage of evolution, prior to the UCH II region phase, or in turn, that their radio continuum emission traces stellar winds and jets in most cases.

The rate of Lyman photons from a young star, which sets the maximum radio luminosity from photo-ionized gas, differs greatly at varying spectral types (continuous line in Fig. 6 B). For

$L_{\text{bol}} < 10^3 L_{\odot}$, young stars are over-luminous with respect to the photo-ionization limit, and the ionization mechanism is likely related to shocks (Curiel et al. 1987, 1989). It has been suggested that a single power-law correlation, which fits together the low ($< 10^3 L_{\odot}$) and high ($> 10^3 L_{\odot}$) bolometric luminosities, implies that a common mechanism, namely shock-ionization, is responsible for the observed radio emission (Anglada 1995; Anglada et al. 2015).

The correlation we prove in Fig. 6 A, between the radio and H₂O maser luminosities, provides an argument in favor of the shock-ionization as opposed to photo-ionization. Since the H₂O maser transition at 22.2 GHz is inverted by shocks, where stellar winds and jets impact ambient gas, it follows that, if the radio continuum emission is also produced by shocks, and both are related to the mechanical energy of the outflow emission, the radio continuum and H₂O maser luminosities should be related⁴. Felli et al. (1992) firstly established a correlation between the H₂O maser luminosity and the mechanical energy of molecular outflow, as measured on parsec scales (see also Sect. 4.4 of Tofani et al. 1995). Here, we revise this correlation with improved confidence, by directly associating H₂O maser spots and radio thermal jets at the smallest scales accessible ($\lesssim 0''.1$), and with accurate absolute positions ($\sim 0''.01$).

5. Conclusions

We report about a multi-frequency VLA survey of radio continuum emission towards a large sample of H₂O maser sites

⁴ We note that, even though masers might be amplifying a background continuum, we exclude a systematic effect on Fig. 6 A for two reasons: (i) 22.2 GHz H₂O masers do not necessarily overlap with the 22 GHz continuum, and (ii) there is no spatial correlation between the 22 GHz continuum brightness and the distribution of the brightest H₂O masers (e.g., Moscadelli et al. 2016).

(36), entitled: the “Protostellar Outflows at the Earliest Stages” (POETS) survey. We extend on the early work by Tofani et al. (1995), with the idea of combining the information on maser lines and free-free continuum, to study the engines of molecular outflows. These observations achieve sensitivities as low as $5 \mu\text{Jy beam}^{-1}$ and probe angular scales as small as $0''.1$.

Our results can be summarized as follows:

1. This is the first systematic survey towards H₂O maser sites conducted at high angular resolution and different frequency bands (C, Ku, and K). At the current sensitivity, the detection rate of 22 GHz continuum emission, within a few 1000 au from the H₂O masers, is 100%.
2. The radio continuum fluxes are well below those expected as due to the Lyman flux of ZAMS stars, suggesting that the young stars exciting the continuum emission are at an early stage of evolution. Spectral indexes (α) between 1 and 7 cm are generally positive and below 1.3; a few sources are associated with optically thin and thick emission at the longer and shorter wavelengths, respectively. These results are consistent with the radio continuum emission tracing the ionized gas component of stellar winds and jets. We discuss a number of scenarios for thermal jet emission, such as in cores with moderate optical depth, surrounded by optically-thin extended emission and knots (e.g., Sects. 4.1–4.4).
3. Radio thermal jets associated with H₂O maser emission show a strong correlation ($r > 0.8$) with both, the isotropic H₂O maser luminosity, and the bolometric luminosity of the young stars (Fig. 6). This seems independent of the spectral type of the young stars. In turn, these findings support the idea that their radio continuum flux is mainly produced through shock-ionization, given that: (i) H₂O masers also trace shocked gas where stellar winds and jets impact ambient gas, and (ii) photo-ionization is not effective for ZAMS stars earlier than B5. Alternatively, we can conclude that H₂O masers are preferred signposts of radio thermal jets, when the stars are not evolved and associated with bright radio continuum ($\gg 1 \text{ mJy}$).

In a following paper in the series, we will study the energetics of (proto)stellar winds and jets, by combining the mass loss rate estimated from the radio continuum observations with the gas kinematics traced by the H₂O maser spots.

Acknowledgements. Comments from an anonymous referee are gratefully acknowledged. The authors thank Sergio Dzib, Carlos Carrasco-González, Mark Reid, Riccardo Cesaroni, and Roberto Galván-Madrid for fruitful discussion in preparation. A.S. gratefully acknowledges financial support by the Deutsche Forschungsgemeinschaft (DFG) Priority Program 1573.

References

Anglada, G. 1995, in *Revista Mexicana de Astronomía y Astrofísica Conference Series*, Vol. 1, *Revista Mexicana de Astronomía y Astrofísica Conference Series*, ed. S. Lizano & J. M. Torrelles, 67

Anglada, G. 1996, in *Astronomical Society of the Pacific Conference Series*, Vol. 93, *Radio Emission from the Stars and the Sun*, ed. A. R. Taylor & J. M. Paredes, 3–14

Anglada, G., Rodríguez, L. F., & Carrasco-González, C. 2015, *Advancing Astrophysics with the Square Kilometre Array (AASKA14)*, 121

Anglada, G., Villuendas, E., Estalella, R., et al. 1998, *AJ*, 116, 2953

Arce, H. G., Shepherd, D., Gueth, F., et al. 2007, *Protostars and Planets V*, 245

Beuther, H., Schilke, P., Sridharan, T. K., et al. 2002, *A&A*, 383, 892

Brunthaler, A., Reid, M. J., Menten, K. M., et al. 2009, *ApJ*, 693, 424

Burns, R. A., Handa, T., Imai, H., et al. 2017, *MNRAS*, 467, 2367

Burns, R. A., Handa, T., Nagayama, T., Sunada, K., & Omodaka, T. 2016, *MNRAS*, 460, 283

Caratti o Garatti, A., Stecklum, B., Garcia Lopez, R., et al. 2017, *Nature Physics*, 13, 276

Carrasco-González, C., Rodríguez, L. F., Anglada, G., et al. 2010, *Science*, 330, 1209

Cesaroni, R., Moscadelli, L., Neri, R., et al. 2018, *ArXiv e-prints [arXiv:1802.04228]*

Chen, H.-R. V., Keto, E., Zhang, Q., et al. 2016, *ApJ*, 823, 125

Churchwell, E. 1999, in *NATO Advanced Science Institutes (ASI) Series C*, Vol. 540, *NATO Advanced Science Institutes (ASI) Series C*, ed. C. J. Lada & N. D. Kylafis, 515

Churchwell, E. 2002, *ARA&A*, 40, 27

Curiel, S., Canto, J., & Rodríguez, L. F. 1987, *Rev. Mexicana Astron. Astrofis.*, 14, 595

Curiel, S., Ho, P. T. P., Patel, N. A., et al. 2006, *ApJ*, 638, 878

Curiel, S., Rodríguez, L. F., Bohigas, J., et al. 1989, *Astrophysical Letters and Communications*, 27, 299

Davies, B., Lumsden, S. L., Hoare, M. G., Oudmaijer, R. D., & de Wit, W.-J. 2010, *MNRAS*, 402, 1504

De Buizer, J. M., Liu, M., Tan, J. C., et al. 2017, *ApJ*, 843, 33

de Wit, W. J., Hoare, M. G., Oudmaijer, R. D., & Lumsden, S. L. 2010, *A&A*, 515, A45

Felli, M., Palagi, F., & Tofani, G. 1992, *A&A*, 255, 293

Frank, A., Ray, T. P., Cabrit, S., et al. 2014, *Protostars and Planets VI*, 451

Furuya, R. S., Kitamura, Y., Wootten, A., Claussen, M. J., & Kawabe, R. 2003, *ApJS*, 144, 71

Galván-Madrid, R., Zhang, Q., Keto, E., et al. 2010, *ApJ*, 725, 17

Goddi, C. & Moscadelli, L. 2006, *A&A*, 447, 577

Goddi, C., Moscadelli, L., & Sanna, A. 2011, *A&A*, 535, L8

Goddi, C., Moscadelli, L., Sanna, A., Cesaroni, R., & Minier, V. 2007, *A&A*, 461, 1027

Goddi, C., Moscadelli, L., Torrelles, J. M., Uscanga, L., & Cesaroni, R. 2006, *A&A*, 447, L9

Hoare, M. G. & Franco, J. 2007, *Astrophysics and Space Science Proceedings*, 1, 61

Hoare, M. G., Kurtz, S. E., Lizano, S., Keto, E., & Hofner, P. 2007, *Protostars and Planets V*, 181

Hofner, P., Cesaroni, R., Olmi, L., et al. 2007, *A&A*, 465, 197

Hollenbach, D., Elitzur, M., & McKee, C. F. 2013, *ApJ*, 773, 70

Hunter, T. R., Brogan, C. L., Bartkiewicz, A., et al. 2018, *ArXiv e-prints [arXiv:1806.06981]*

Johnston, K. G., Shepherd, D. S., Robitaille, T. P., & Wood, K. 2013, *A&A*, 551, A43

Marti, J., Rodríguez, L. F., & Reipurth, B. 1993, *ApJ*, 416, 208

Maud, L. T., Hoare, M. G., Galván-Madrid, R., et al. 2017, *MNRAS*, 467, L120

Maud, L. T., Moore, T. J. T., Lumsden, S. L., et al. 2015, *MNRAS*, 453, 645

Moscadelli, L., Cesaroni, R., Rioja, M. J., Dodson, R., & Reid, M. J. 2011, *A&A*, 526, A66

Moscadelli, L., Li, J. J., Cesaroni, R., et al. 2013, *A&A*, 549, A122

Moscadelli, L., Reid, M. J., Menten, K. M., et al. 2009, *ApJ*, 693, 406

Moscadelli, L., Sánchez-Monge, Á., Goddi, C., et al. 2016, *A&A*, 585, A71

Panagia, N. & Felli, M. 1975, *A&A*, 39, 1

Purser, S. J. D., Lumsden, S. L., Hoare, M. G., et al. 2016, *MNRAS*, 460, 1039

Qiu, K., Zhang, Q., Wu, J., & Chen, H.-R. 2009, *ApJ*, 696, 66

Rau, U. & Cornwell, T. J. 2011, *A&A*, 532, A71

Reid, M. J., Menten, K. M., Brunthaler, A., et al. 2014, *ApJ*, 783, 130

Rengarajan, T. N. & Ho, P. T. P. 1996, *ApJ*, 465, 363

Reynolds, S. P. 1986, *ApJ*, 304, 713

Rodríguez, L. F., Garay, G., Curiel, S., et al. 1994, *ApJ*, 430, L65

Rodríguez, L. F., Moran, J. M., Ho, P. T. P., & Gottlieb, E. W. 1980, *ApJ*, 235, 845

Rodríguez-Kamenetzky, A., Carrasco-González, C., Araudo, A., et al. 2017, *ApJ*, 851, 16

Rosero, V., Hofner, P., Claussen, M., et al. 2016, *ApJS*, 227, 25

Rygl, K. L. J., Brunthaler, A., Sanna, A., et al. 2012, *A&A*, 539, A79

Sanna, A., Cesaroni, R., Moscadelli, L., et al. 2014, *A&A*, 565, A34

Sanna, A., Moscadelli, L., Cesaroni, R., et al. 2016, *A&A*, 596, L2

Sanna, A., Moscadelli, L., Cesaroni, R., et al. 2010a, *A&A*, 517, A71

Sanna, A., Moscadelli, L., Cesaroni, R., et al. 2010b, *A&A*, 517, A78

Sanna, A., Reid, M. J., Carrasco-González, C., et al. 2012, *ApJ*, 745, 191

Tanaka, K. E. I., Tan, J. C., & Zhang, Y. 2016, *ApJ*, 818, 52

Thompson, R. I. 1984, *ApJ*, 283, 165

Tofani, G., Felli, M., Taylor, G. B., & Hunter, T. R. 1995, *A&AS*, 112, 299

Torrelles, J. M., Patel, N. A., Anglada, G., et al. 2003, *ApJ*, 598, L115

van der Tak, F. F. S. & Menten, K. M. 2005, *A&A*, 437, 947

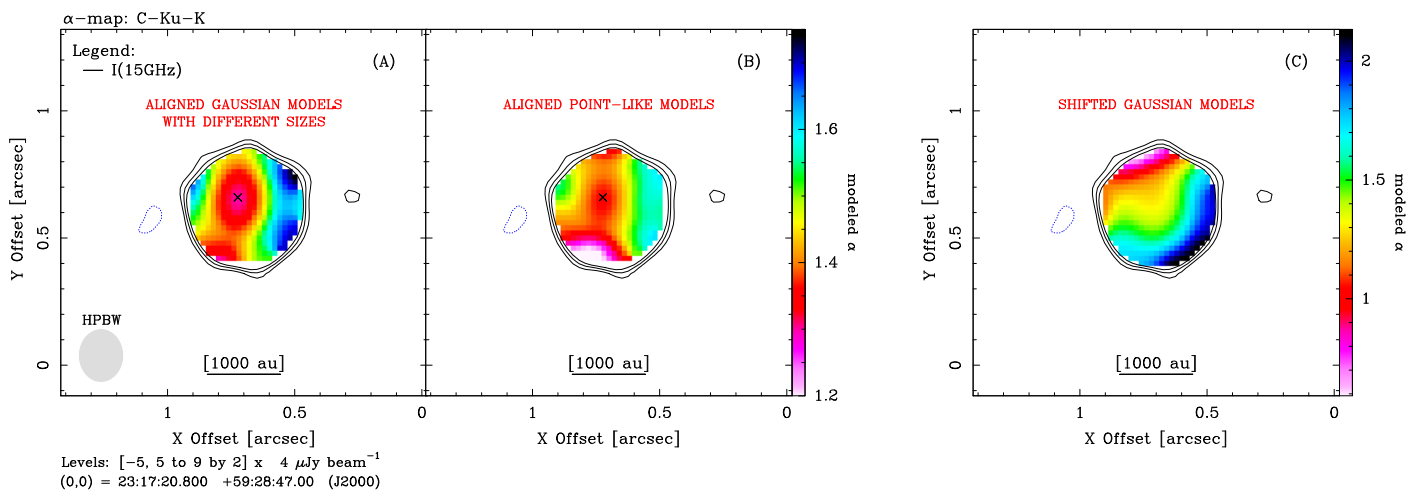


Fig. A.1. Simulated spectral index maps for field G111.24–1.24 in Fig. 5 (Sect. A). Labels and symbols as in Fig. 1. Panels A, B, and C show the spectral index maps (colors) obtained assuming three different source models at C, Ku, and K bands. Black contours are those of the observed average brightness map for a direct comparison with Fig. 5. The cross in panels A and B marks the peak position of the observed C-band emission.

Appendix A: Variations in the spectral index maps

In Fig. 5, the spectral index maps which we produced by combining observations at different frequency bands show regular gradients across the radio continuum emission. Here, we show that these gradients can be produced by small position shifts between the radio continuum maps at the different frequencies.

As an example, we make use of the tasks *simobserve* and *clean* of CASA, in order to simulate the spectral index map observed for the field G111.24–1.24 (Fig. 5). The radio continuum emission in G111.24–1.24 is compact with respect to the VLA beam at the different frequencies (column 4 of Table 3). We used the CASA toolkit to set the source model at the C, Ku, and K bands separately, and assume that the source has a Gaussian brightness distribution, with flux densities at each frequency from column 10 of Table 3.

First, we considered a case where the source size is scaled to a third of the beam at each frequency. We also aligned the Gaussian peaks at the peak position of the C-band emission (columns 6 and 7 of Table 3). We then simulated the *uv*-datasets at each frequency with the task *simobserve* of CASA, under the same conditions of our observations (Table 2) but setting a long integration time, so that the spectral index maps are not limited by sensitivity.

In panel A of Fig. A.1, we show the modeled spectral index map cleaned with the same parameters of the observed map (Sect. 3.3). To help the comparison with Fig. 5, we also draw the contours of the observed average brightness map. The modeled spectral index map ranges from 1.2 to 1.7, up to 3σ from the (average) spectral index computed with the integrated fluxes (1.1 ± 0.2). Close to the C-band peak (cross), and along the beam major axis, spectral index values are within 1σ of the average spectral index. For further comparison, we repeated the procedure assuming point-like emission at each frequency (panel B), but all other parameters being equal. We found that the spectral index distribution did not change significantly from panels A to B.

Finally, in panel C of Fig. A.1, we show a third case where we shifted the peak positions at each frequency according to columns 6 and 7 of Table 3. The largest offset of $0''.07$, between the C- and Ku-band peaks, is within the uncertainty of the calibration. The source size was scaled to a third of the beam at each frequency. The modeled spectral index map spans a larger range

of values, from 0.6 to 2.1, and shows a regular gradient from the southwest to the northeast. This gradient is approximately the same as in the observed map, demonstrating that it is caused by the small offsets between the continuum maps at different frequencies.

This example shows that one has to exert caution when interpreting spectral index gradients in the α -maps.

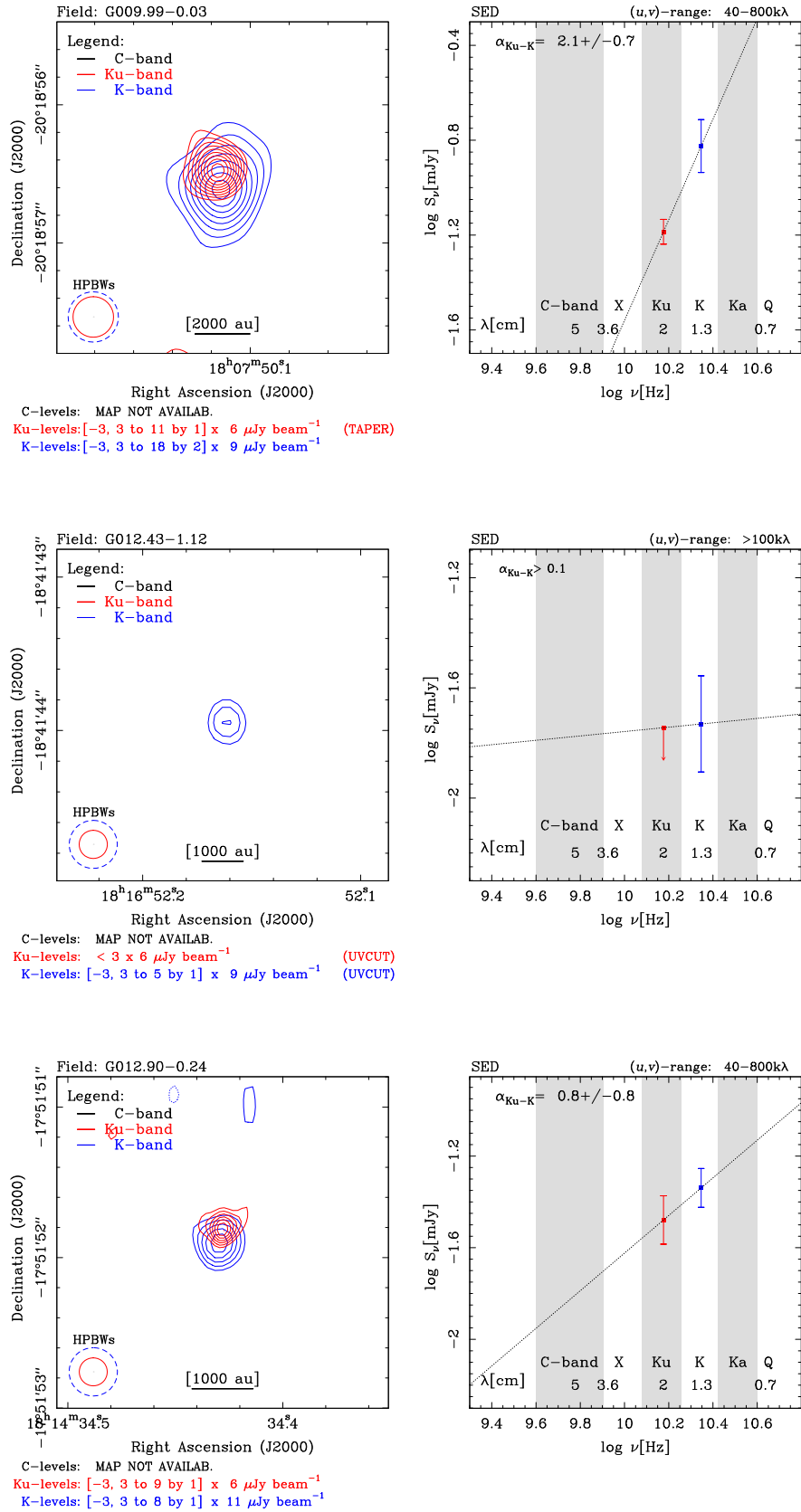


Fig. 5. For each source in Table 1, analysis of the VLA radio continuum emission associated with the H₂O maser sites. Labels and symbols as in Figs. 1–4.

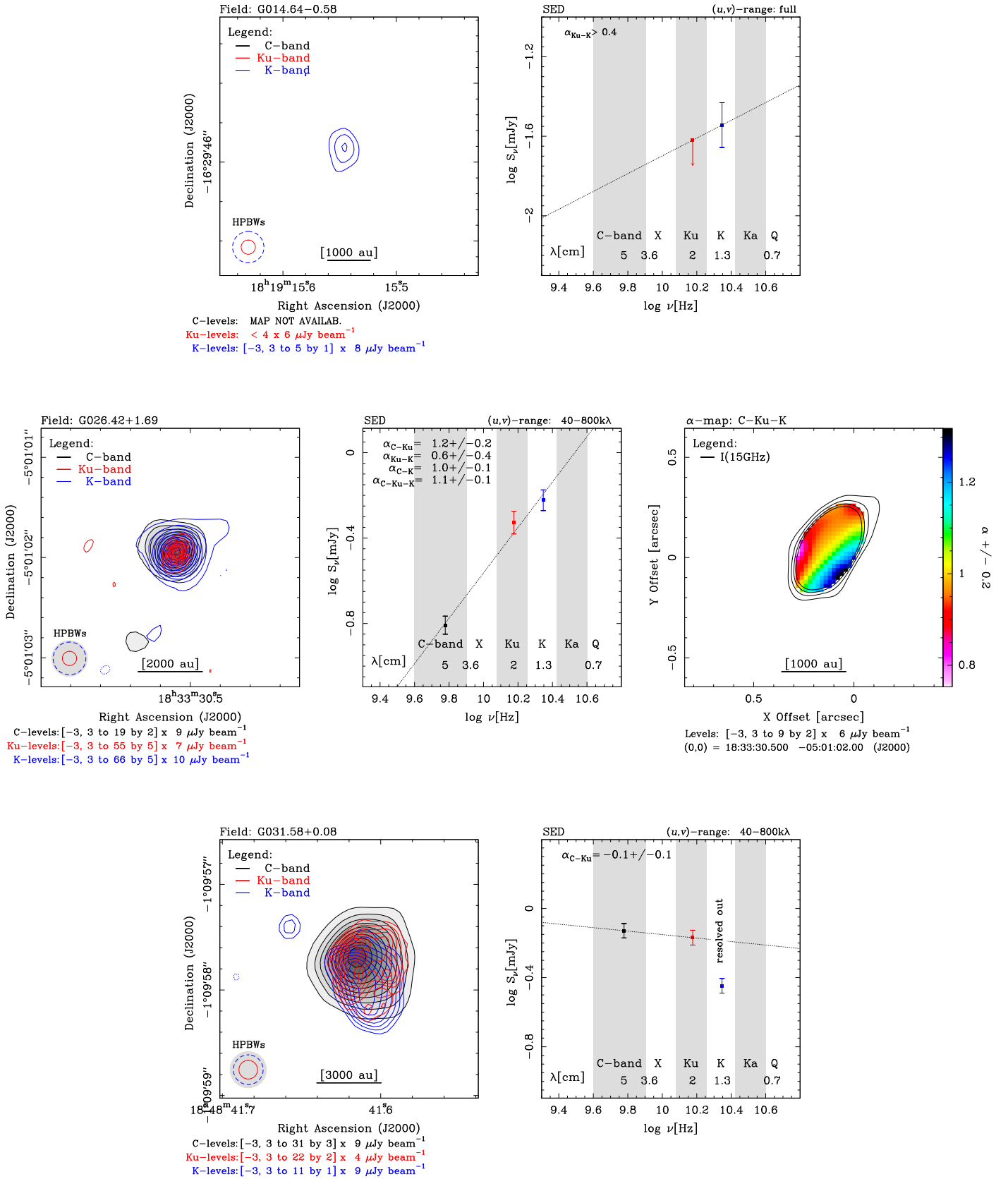


Fig. 5. (Continued)

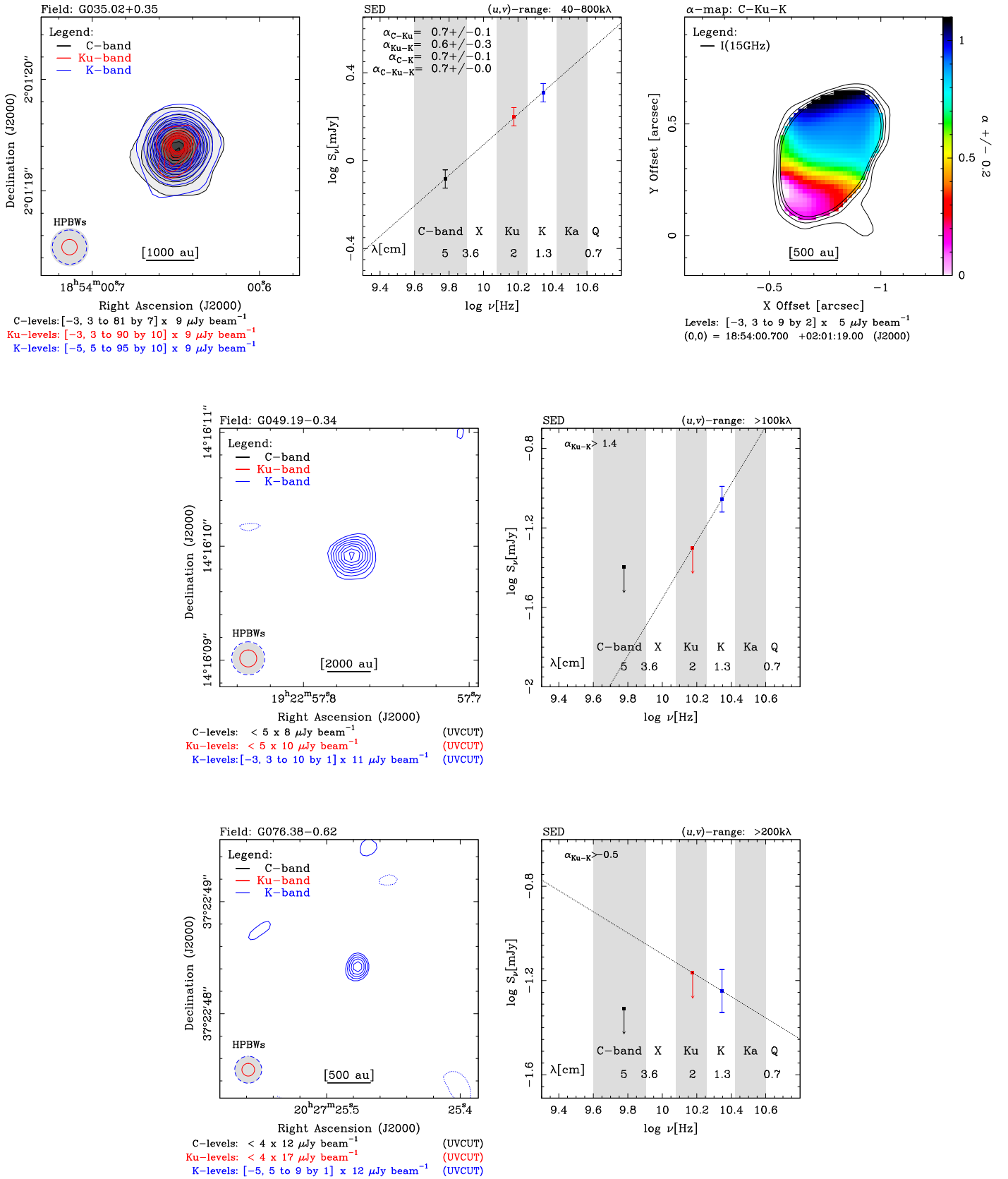


Fig. 5. (Continued)

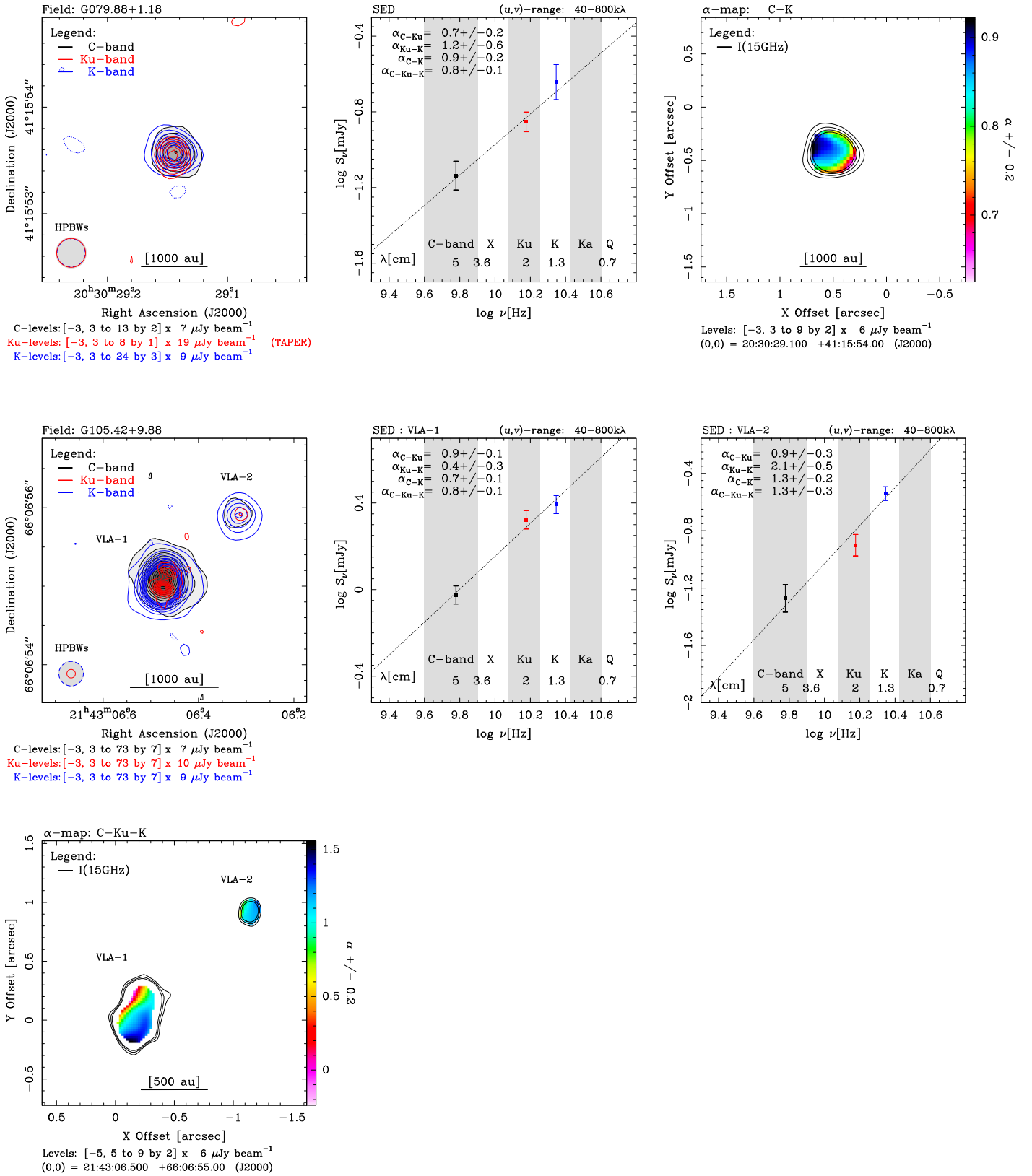


Fig. 5. (Continued)

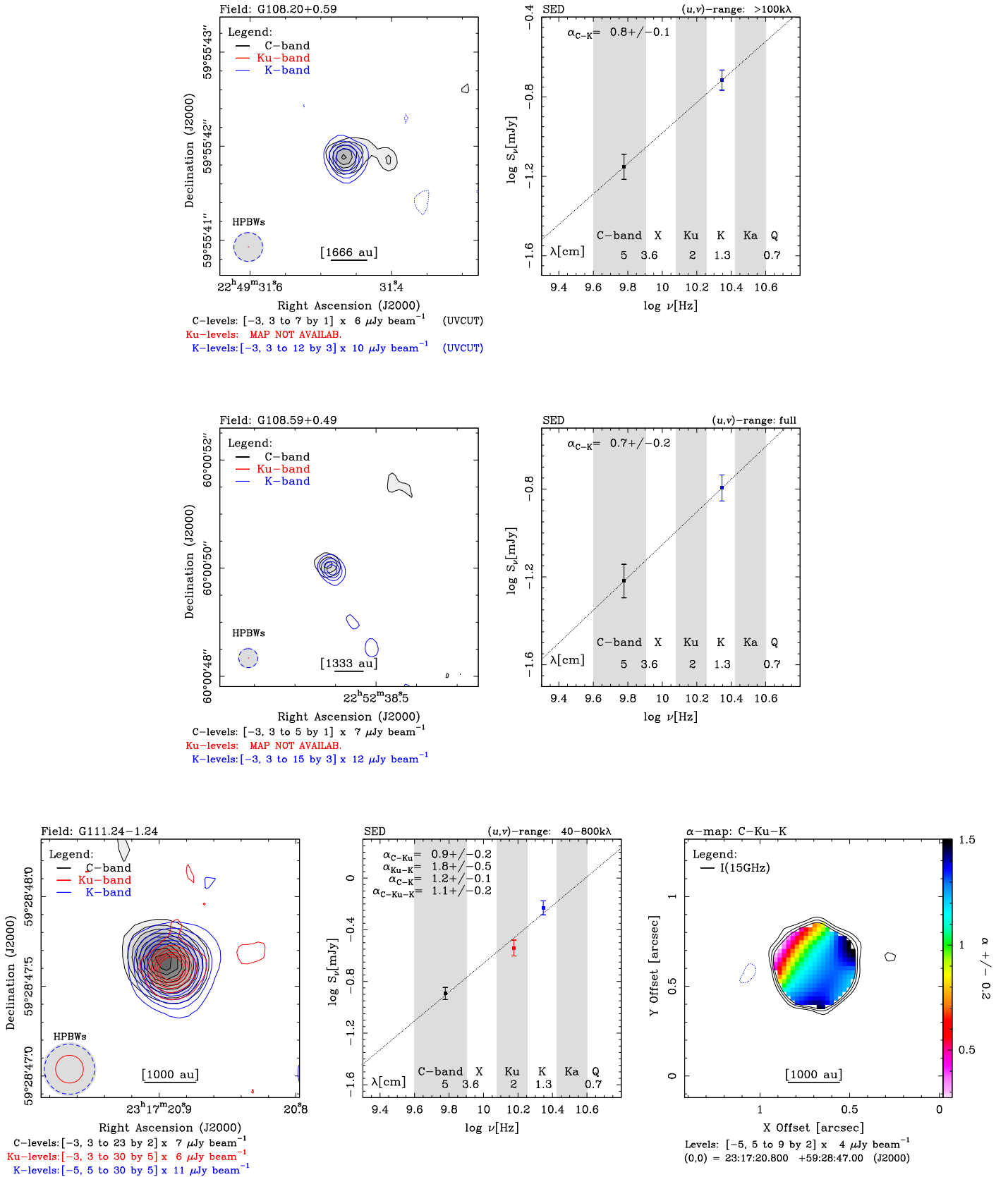


Fig. 5. (Continued)

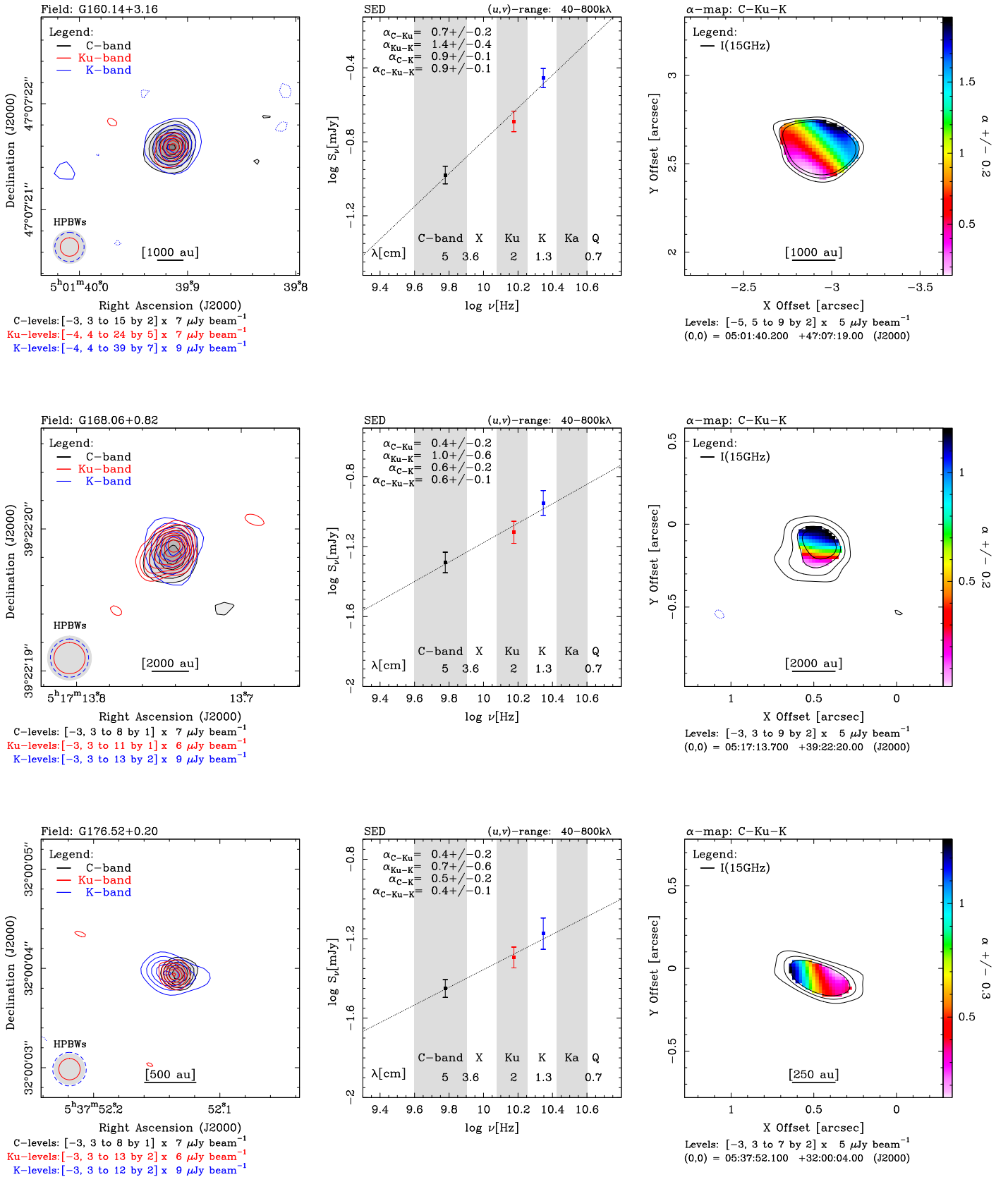


Fig. 5. (Continued)

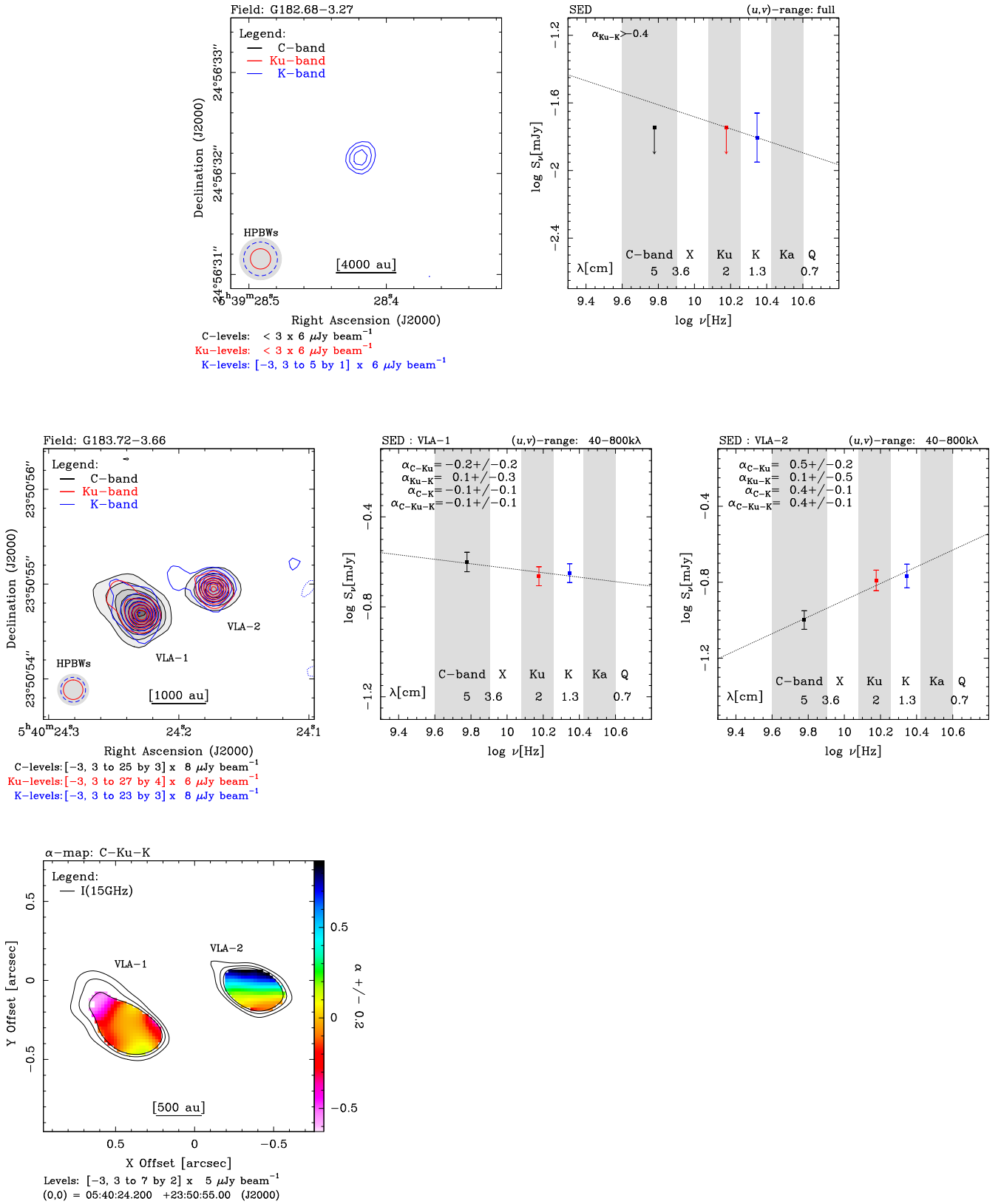


Fig. 5. (Continued)

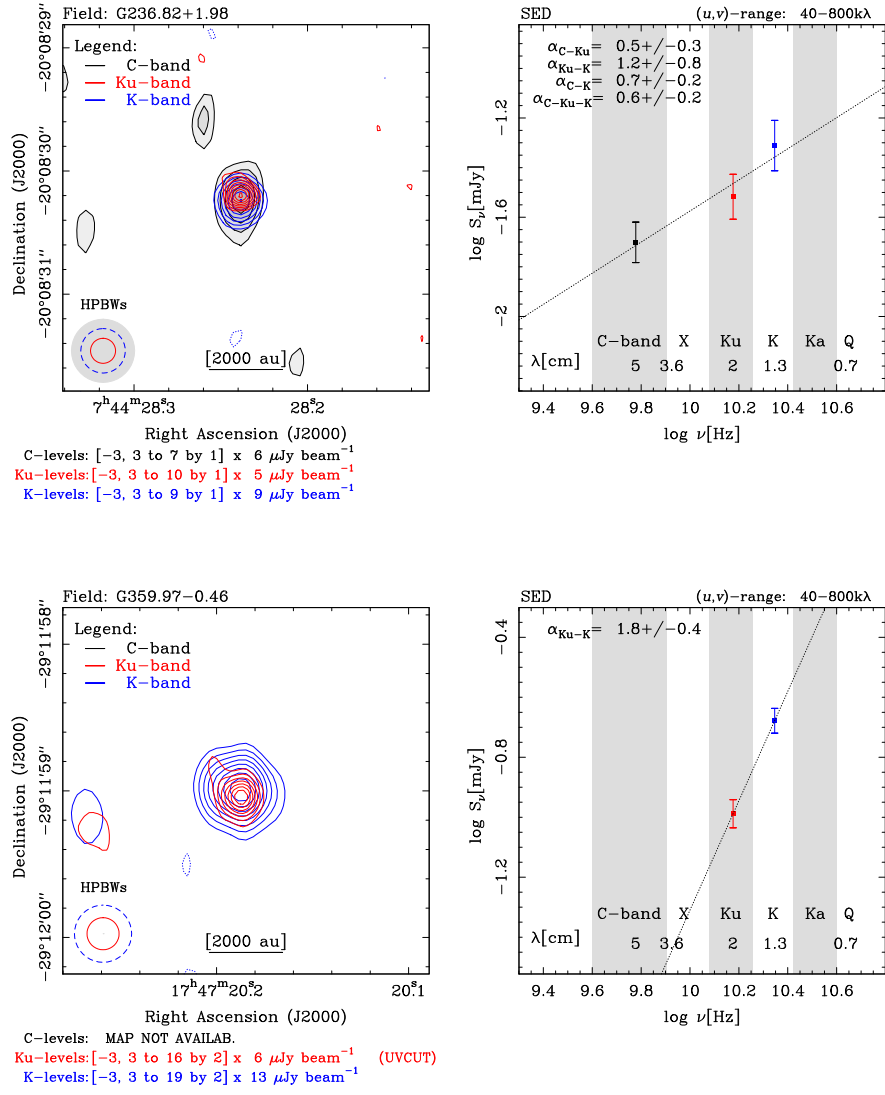


Fig. 5. (Continued)

Table 3. Properties of the radio continuum sources.

Field	Component	Band	HPBW ($''$)	rms (mJy beam $^{-1}$)	R.A. (J2000) (h:m:s)	Dec. (J2000) ($^{\circ}$:' $''$)	I_{pix} (mJy beam $^{-1}$)	Size	S_{int}^{SED} (mJy)	α	Type
(1)	(2)	(3)	(4)	(5)	(6)	(7)	(8)	(9)	(10)	(11)	(12)
G009.99–0.03 ⁵	VLA-1 ⁶	Ku K	0.293 0.364	0.006 0.009	18:07:50.117 18:07:50.114	–20:18:56.48 –20:18:56.60	0.070 0.162	SR SR	0.065 0.150	+2.1 ± 0.7	OP
G012.43–1.12 ^{a,b}	VLA-1 ⁷	Ku K	0.184 0.313	0.006 0.009	< 0.018 0.019	> 0.1	NA
G012.90–1.12	VLA-1	Ku K	0.186 0.321	0.006 0.011	18:14:34.427 18:14:34.428	–17:51:51.82 –17:51:51.90	0.054 0.086	SR C	0.033 0.046	+0.8 ± 0.8	SW
G012.91–0.26 ⁸	VLA-1	C	0.358	0.013	18:14:39.511	–17:52:00.10	0.420	SR/C	0.441	+1.3 ± 0.1	JET
		K	0.325	0.011	18:14:39.509	–17:52:00.18	2.074	C	1.944/2.668 ⁹		
	VLA-2	C	0.358	0.013	18:14:39.553	–17:52:01.24	0.223	SR	0.197	–0.1 ± 0.1	
		K	0.325	0.011	18:14:39.551	–17:52:01.32	0.184	SR	0.181/0.157 ¹⁰		
G014.64–0.58 ^b	VLA-1	Ku K	0.180 0.398	0.006 0.008	< 0.024 0.029	> 0.4	NA
G026.42+1.69	VLA-1	C Ku K	0.356 0.142 0.327	0.009 0.007 0.010	18:33:30.508 18:33:30.508 18:33:30.508	–05:01:01.94 –05:01:01.94 –05:01:01.94	0.179 0.390 0.663	SR SR C	0.156 0.470 0.599	+1.1 ± 0.1	SW
G031.58+0.08 ^{b, 11}	VLA-1	C Ku K	0.343 0.177 0.282	0.009 0.005 0.010	18:48:41.616 18:48:41.618 18:48:41.616	–01:09:57.68 –01:09:57.62 –01:09:57.80	0.292 0.112 0.110	R R R	0.743 0.678 0.357 ¹²	–0.1 ± 0.1	H II
G035.02+0.35 ^a	VLA-1	C Ku K	0.338 0.138 0.308	0.009 0.009 0.009	18:54:00.648 18:54:00.649 18:54:00.648	02:01:19.36 02:01:19.42 02:01:19.42	0.733 1.140 1.872	SR R C	0.825 1.584 2.036	+0.69 ± 0.02	JET
G049.19–0.34 ^b	VLA-1 ¹³	C Ku K	0.271 0.149 0.291	0.008 0.010 0.011	< 0.040 < 0.050 0.088	> 1.4	NA

⁵ The 8 GHz flux of this source was extrapolated assuming an optically-thin spectral index, by analogy with Sect. 4.2.⁶ Tapering of 500 k λ at Ku band.⁷ Maps cleaned with uv -cut: > 100 k λ ⁸ C-band data are from exp. 12B-044, and are centered at the frequency of 6.240 GHz.⁹ Fluxes at the frequencies of 20.2 and 24.2 GHz, respectively.¹⁰ Fluxes at the frequencies of 20.2 and 24.2 GHz, respectively.¹¹ This source was excluded from Fig. 6 A because it is not a thermal jet.¹² Resolved out/missing flux¹³ Maps cleaned with uv -cut: > 100 k λ

Table 3. continued.

Field (1)	Component (2)	Band (3)	HPBW ($''$) (4)	rms (mJy beam $^{-1}$) (5)	R.A. (J2000) (h:m:s) (6)	Dec. (J2000) ($^{\circ}$: $''$) (7)	I_{pix} (mJy beam $^{-1}$) (8)	Size (9)	S_{int}^{SED} (mJy) (10)	α (11)	Type (12)
G076.38–0.62 ^{a,b}	VLA-1 ¹⁴	C	0.236	0.012	< 0.048		
		Ku	0.113	0.017	< 0.068	> -0.5	NA
		K	0.241	0.012	20:27:25.477	37:22:48.40	0.119	C	0.057		
G079.88+1.18	VLA-1 ¹⁵	C	0.288	0.007	20:30:29.143	41:15:53.58	0.093	SR	0.073	+0.8 ± 0.1	SW
		Ku	0.272	0.019	20:30:29.144	41:15:53.55	0.166	SR/C	0.140		
		K	0.265	0.009	20:30:29.144	41:15:53.55	0.258	C	0.228		
G090.21+2.32	VLA-1	C	0.292	0.006	21:02:22.703	50:03:08.30	0.130	R	0.153/0.150 ¹⁶	-0.1 ± 0.1	JET
		Ku	0.166	0.006	21:02:22.706	50:03:08.27	0.091	R	0.137		
		K	0.285	0.010	21:02:22.700	50:03:08.27	0.354	SR/C	0.378/0.475 ¹⁷	+2.5 ± 0.5	OP
G105.42+9.88	VLA-1	C	0.315	0.007	21:43:06.470	66:06:55.06	0.579	SR	0.944	+0.8 ± 0.1	JET
		Ku	0.110	0.010	21:43:06.474	66:06:54.98	0.898	R	2.100		
		K	0.313	0.009	21:43:06.480	66:06:55.00	1.917	SR	2.477		
	VLA-2	C	0.315	0.007	21:43:06.322	66:06:55.96	0.045	SR	0.053	+1.3 ± 0.3	SW
		Ku	0.110	0.010	21:43:06.312	66:06:55.92	0.112	SR	0.126		
		K	0.313	0.009	21:43:06.312	66:06:55.90	0.298	C	0.288		
G108.20+0.59	VLA-1 ¹⁸	C	0.317	0.006	22:49:31.468	59:55:41.88	0.044	R	0.070	+0.8 ± 0.1	SW
		K	0.306	0.010	22:49:31.468	59:55:41.88	0.179	SR	0.193		
G108.59+0.49	VLA-1	C	0.377	0.007	22:52:38.620	60:00:50.08	0.037	SR	0.060	+0.7 ± 0.2	SW
		K	0.350	0.012	22:52:38.612	60:00:49.96	0.176	C	0.160		
G111.24–1.24	VLA-1	C	0.296	0.007	23:17:20.895	59:28:47.66	0.143	C	0.128	+1.1 ± 0.2	SW
		Ku	0.155	0.006	23:17:20.891	59:28:47.60	0.270	C	0.288		
		K	0.279	0.011	23:17:20.892	59:28:47.60	0.669	C	0.589		
G160.14+3.16	VLA-1	C	0.311	0.007	05:01:39.918	47:07:21.58	0.109	C	0.105	+0.9 ± 0.1	SW
		Ku	0.174	0.007	05:01:39.914	47:07:21.60	0.184	SR	0.204		
		K	0.276	0.009	05:01:39.912	47:07:21.64	0.349	C	0.351		
G168.06+0.82	VLA-1	C	0.311	0.007	05:17:13.741	39:22:19.82	0.055	SR	0.051	+0.6 ± 0.1	JET
		Ku	0.220	0.006	05:17:13.741	39:22:19.88	0.065	R	0.076		
		K	0.269	0.009	05:17:13.741	39:22:19.88	0.116	SR	0.112		

¹⁴ Maps cleaned with uv -cut: > 200 k λ ¹⁵ Tapering of 500 k λ at Ku band.¹⁶ Fluxes at the frequencies of 5.0 and 7.0 GHz, respectively.¹⁷ Fluxes at the frequencies of 20.2 and 24.2 GHz, respectively.¹⁸ Maps cleaned with uv -cut: > 100 k λ

Table 3. continued.

Field (1)	Component (2)	Band (3)	HPBW ($''$) (4)	rms (mJy beam $^{-1}$) (5)	R.A. (J2000) (h:m:s) (6)	Dec. (J2000) ($^{\circ}$: $''$) (7)	I_{pix} (mJy beam $^{-1}$) (8)	Size (9)	S_{int}^{SED} (mJy) (10)	α (11)	Type (12)
G176.52+0.20	VLA-1	C	0.310	0.007	05:37:52.131	32:00:03.95	0.055	C	0.035	+0.4 \pm 0.1	SW
		Ku	0.215	0.006	05:37:52.136	32:00:03.94	0.080	C	0.051		
		K	0.338	0.009	05:37:52.143	32:00:03.95	0.102	SR/C	0.067		
G182.68–3.27 ^b	VLA-1	C	0.416	0.006	< 0.018		
		Ku	0.201	0.006	< 0.018	> -0.4	NA
		K	0.335	0.006	05:39:28.418	24:56:32.18	0.034	C	0.016		
G183.72–3.66 ¹⁹	VLA-1	C	0.329	0.008	05:40:24.231	23:50:54.70	0.203	R	0.251	-0.1 \pm 0.1	JET
		Ku	0.206	0.006	05:40:24.228	23:50:54.67	0.162	R	0.217		
		K	0.262	0.008	05:40:24.231	23:50:54.70	0.171	SR	0.224		
	VLA-2	C	0.329	0.008	05:40:24.174	23:50:54.94	0.121	C	0.100	+0.4 \pm 0.1	SW
		Ku	0.206	0.006	05:40:24.174	23:50:54.94	0.171	C	0.162		
		K	0.262	0.008	05:40:24.174	23:50:54.94	0.187	C	0.171		
G229.57+0.15 ²⁰	VLA-1	C	0.481	0.006	07:23:01.845	-14:41:32.76	0.064	SR	0.054	+0.68 \pm 0.02	SW
		Ku	0.194	0.005	07:23:01.845	-14:41:32.79	0.108	SR	0.100		
		K	0.412	0.007	07:23:01.845	-14:41:32.82	0.168	C	0.134		
	VLA-2	C	0.481	0.006	07:23:01.804	-14:41:32.88	0.039	SR	0.027	+1.2 \pm 0.1	SW
		Ku	0.194	0.005	07:23:01.804	-14:41:32.94	0.099	C	0.078		
		K	0.412	0.007	07:23:01.804	-14:41:32.94	0.179	C	0.137		
	VLA-3	C	0.481	0.006	07:23:01.825	-14:41:31.50	0.037	R	0.047	+0.0 \pm 0.1	JET
		K	0.412	0.007	07:23:01.821	-14:41:31.80	0.032	R	0.046		
G236.82+1.98	VLA-1	C	0.513	0.006	07:44:28.238	-20:08:30.24	0.040	C	0.020	+0.6 \pm 0.2	SW
		Ku	0.203	0.005	07:44:28.238	-20:08:30.21	0.052	SR	0.030		
		K	0.361	0.009	07:44:28.238	-20:08:30.24	0.082	C	0.049		
G240.32+0.07 ^{a, 21}	VLA-1	C	0.374	0.013	07:44:52.036	-24:07:42.16	9.611	R/SR	12.533	...	H II
		Ku	0.199	0.007	07:44:52.042	-24:07:42.19	5.871	R	14.306		
		K	0.370	0.016	07:44:52.031	-24:07:42.16	9.848	R/SR	13.461		
	VLA-2	C	0.374	0.013	07:44:51.975	-24:07:42.40	0.303	SR	0.335	+0.84 \pm 0.03	JET
		Ku	0.199	0.007	07:44:51.977	-24:07:42.40	0.361	R	0.725		
		K	0.370	0.016	07:44:51.970	-24:07:42.34	0.764	SR	1.005		NA
	VLA-3	Ku	0.199	0.007	07:44:52.071	-24:07:41.87	0.122	C	0.137		NA
	VLA-4	Ku	0.199	0.007	07:44:51.950	-24:07:42.58	0.062	C	0.090		NA

¹⁹ H₂O masers are associated with VLA-1.²⁰ H₂O maser luminosities are $0.3 \cdot 10^{-5}$ and $0.4 \cdot 10^{-5} L_{\odot}$ for VLA-1 and VLA-2, respectively. For the purpose of Fig. 6 B, the bolometric luminosity was split between VLA-1 and VLA-2.²¹ Since H₂O masers are associated with VLA-2, only this component was considered in Fig. 6 A.

Table 3. continued.

Field	Component	Band	HPBW (")	<i>rms</i> (mJy beam ⁻¹)	R.A. (J2000) (h m s)	Dec. (J2000) (° ′ ″)	<i>I_{pix}</i> (mJy beam ⁻¹)	Size	<i>S_{int}^{SED}</i> (mJy)	α	Type
(1)	(2)	(3)	(4)	(5)	(6)	(7)	(8)	(9)	(10)	(11)	(12)
G359.97–0.46 ^{a, 22, 23}	VLA-1	Ku	0.219	0.006	17:47:20.186	–29:11:59.03	0.101	SR	0.103	+1.8 ± 0.4	OP
		K	0.390	0.013	17:47:20.189	–29:11:59.00	0.248	C	0.210		

Notes. Radio continuum sources have been classified as follows (column 12): stellar winds (SW), jets (JET), opaque cores (OP, by analogy with Sect. 4.2), and H II regions (H II). Sources detected at one frequency only have not been classified (NA). ^(a) Sources excluded from Fig. 6 B; *L_{bol}* is uncertain due to high multiplicity in the field. ^(b) Since these sources were only detected at K band, and a reliable estimate of the 8 GHz flux is not available, they were excluded from the analysis in Fig. 6.

²² The Ku-band map was cleaned with *uv*-cut: > 40 kλ

²³ The 8 GHz flux of this source was extrapolated assuming an optically-thin spectral index, by analogy with Sect. 4.2.

Table 4. Bolometric, H₂O maser, and radio luminosities of prototypical jets associated with H₂O maser sites (Fig. 6; cyan circles).

Source	D (kpc)	L _{bol} (10 ⁴ L _⊙)	L _{H₂O} (10 ⁻⁵ L _⊙)	L _{8GHz} (mJy kpc ²)	References
Cepheus A HW2	0.7	2.4	4.50	3.24	1,2,3,4,5
HH 80-81	1.7	1.7	1.41	8.47	6,3,7,8,9
IRAS 20126	1.6	1.3	0.39	0.38	10,2,11,12
S255 NIRS3	1.8	2.9	0.42	3.28	13,14,15,16
AFGL 5142 MM1	2.1	...	0.86	3.33	17,15,18,19
AFGL 2591 VLA-3	3.3	23	1.20	16.15	20,21,22
G023.01-0.41	4.6	4.0	6.46	8.97	23,24,25,26,27

Notes. Sources are listed by increasing heliocentric distance. Column 2: distances to the Sun. Column 3: bolometric luminosities associated with (and dominated by) individual young stars. For region AFGL 5142, a reliable estimate of the bolometric luminosity for source MM1 is not available, and this source has not been plotted in Fig. 6 B. Column 4: H₂O maser luminosities for Cepheus A HW2 and HH 80-81 are from Furuya et al. (2003); all other values have been obtained from accurate VLBA measurements that our group have conducted in the recent years. Column 5: radio continuum luminosities at 8 GHz. Column 6: references to the papers used for estimating values in columns 2–5.

References. (1) Moscadelli et al. (2009); (2) De Buizer et al. (2017); (3) Furuya et al. (2003); (4) Rodríguez et al. (1994); (5) Curiel et al. (2006); (6) Rodríguez et al. (1980); (7) Martí et al. (1993); (8) Carrasco-González et al. (2010); (9) Rodríguez-Kamenetzky et al. (2017); (10) Moscadelli et al. (2011); (11) Chen et al. (2016); (12) Hofner et al. (2007); (13) Burns et al. (2016); (14) Caratti o Garatti et al. (2017); (15) Goddi et al. (2007); (16) Cesaroni et al. (2018); (17) Burns et al. (2017); (18) Goddi & Moscadelli (2006); (19) Goddi et al. (2011) (20) Rygl et al. (2012); (21) Sanna et al. (2012); (22) Johnston et al. (2013); (23) Brunthaler et al. (2009); (24) Sanna et al. (2014); (25) Sanna et al. (2010b); (26) Sanna et al. (2016); (27) Rosero et al. (2016).